Volume 53
Number 31
21 August 2024
Pages 12801-13218

Dalton Transactions

An international journal of inorganic chemistry

rsc.li/dalton

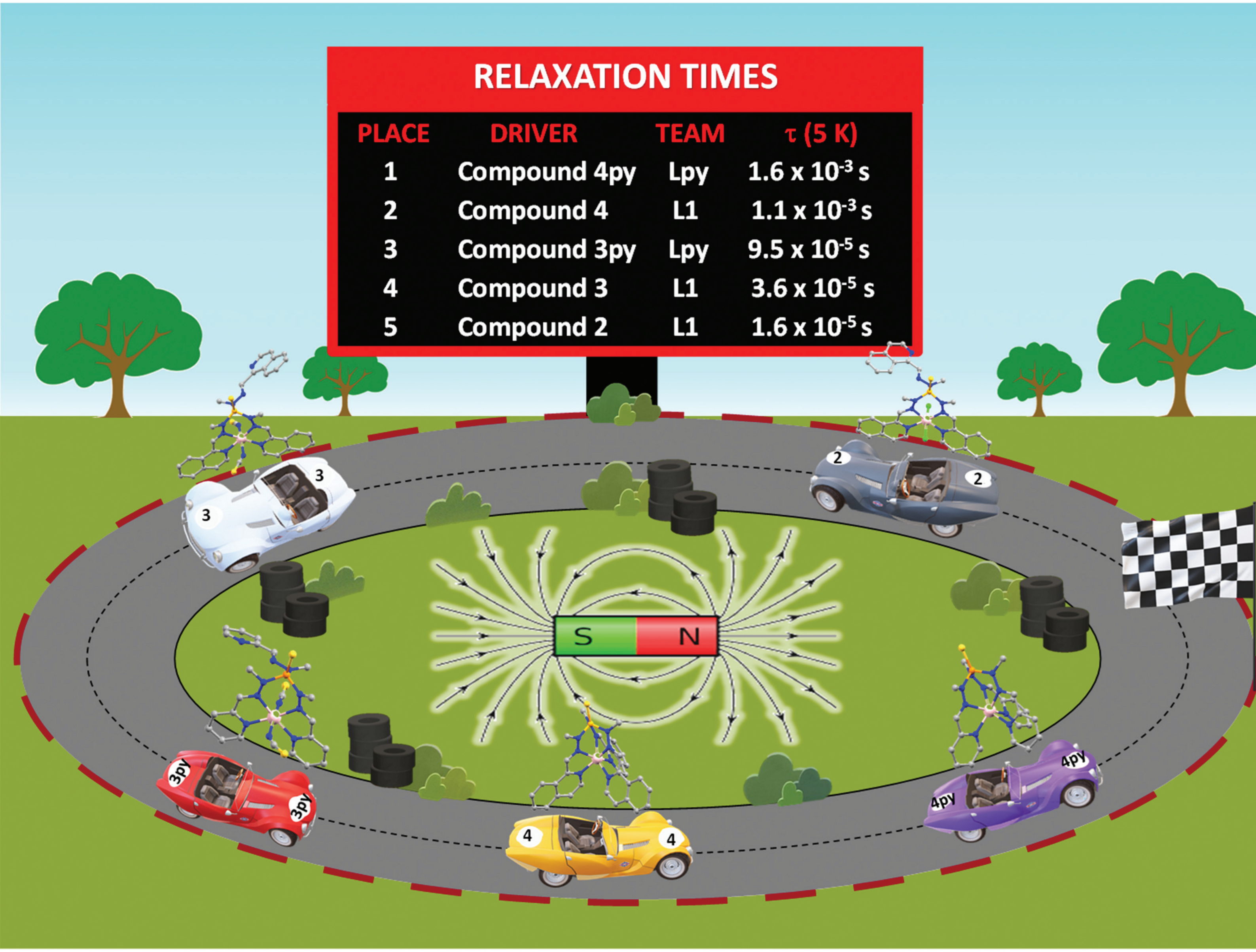

RELAXATION TIMES

PLACE	DRIVER	TEAM	τ (5 K)
1	Compound 4py	Lpy	1.6×10^{-3} s
2	Compound 4	L1	1.1×10^{-3} s
3	Compound 3py	Lpy	9.5×10^{-5} s
4	Compound 3	L1	3.6×10^{-5} s
5	Compound 2	L1	1.6×10^{-5} s

ISSN 1477-9226

ROYAL SOCIETY OF CHEMISTRY

PAPER
Enrique Colacio *et al.*
Control of the geometry and anisotropy driven by the combination of steric and anion coordination effects in Co^{II} complexes with N_6-tripodal ligands: the impact of the size of the ligand on the magnetization relaxation time

Dalton Transactions

PAPER

Cite this: *Dalton Trans.*, 2024, **53**, 12876

Control of the geometry and anisotropy driven by the combination of steric and anion coordination effects in Co^{II} complexes with N_6-tripodal ligands: the impact of the size of the ligand on the magnetization relaxation time†

Aritz Landart,[a] María Mar Quesada-Moreno,[b] María A. Palacios,*[a] Yanling Li,[c] Mykhaylo Ozerov,[d] J. Krzystek[d] and Enrique Colacio*[a]

Four mononuclear Co^{II} complexes of formula $[Co(\mathbf{L})(SCN)_2(CH_3OH)_{0.5}(H_2O)_{0.5}]\cdot 1.5H_2O\cdot 0.75CH_3OH$ (**1**), $[Co(\mathbf{L1})Cl_2]\cdot H_2O\cdot 2CH_3CN$ (**2**), $[Co(\mathbf{L1})(SCN)_2]\cdot 1.5H_2O\cdot CH_3OH$ (**3**) and $[Co(\mathbf{L1})]ClO_4\cdot 2CH_3OH$ (**4**) were prepared from the N_6-tripodal Schiff base ligands $(S)P[N(Me)N{=}C(H)2\text{-}Q]_3$ (**L**) and $(S)P[N(Me)N{=}C(H)1\text{-}ISOQ]_3$ (**L1**), where Q and ISOQ represent quinolyl and isoquinolyl moieties, respectively. In **1**, the **L** ligand does not coordinate to the Co^{II} ion in a tripodal manner but using a new N,N,S tridentate mode, which is due to the fact that the N_6-tripodal coordination promotes a strong steric hindrance between the quinolyl moieties. However, **L1** can coordinate to the Co^{II} ions either in a tripodal manner using Co^{II} salts with poorly coordinating anions to give **4** or in a bisbidentate fashion using Co^{II} salt-containing medium to strongly coordinating anions to afford **2** and **3**. In the case of **L1**, there is no steric hindrance between ISOQ moieties after coordination to the Co^{II} ion. The Co^{II} ion exhibits a distorted octahedral geometry for compounds **1–3**, with the anions in *cis* positions for the former and in *trans* positions for the two latter compounds. Compound **4** shows an intermediate geometry between an octahedral and trigonal prism but closer to the latter one. DC magnetic properties, HFEPR and FIRMS measurements and *ab initio* calculations demonstrate that distorted octahedral complexes **1–3** exhibit easy-plane magnetic anisotropy ($D > 0$), whereas compound **4** shows large easy-axis magnetic anisotropy ($D < 0$). Comparative analysis of the magneto-structural data underlines the important role that is played not only by the coordination geometry but also the electronic effects in determining the anisotropy of the Co^{II} ions. Compounds **2–3** show a field-induced slow relaxation of magnetization. Despite its large easy-axis magnetic anisotropy, compound **4** does not show significant slow relaxation (SMR) above 2 K under zero applied magnetic fields, but its magnetic dilution with Zn^{II} triggers SMR at zero field. Finally, it is worth remarking that compounds **2–4** show smaller relaxation times than the analogous complexes with the tripodal ligand bearing in its arms pyridine instead of isoquinoline moieties, which is most likely due to the increase of the molecular size in the former one.

Received 1st March 2024,
Accepted 22nd April 2024

DOI: 10.1039/d4dt00622d

rsc.li/dalton

Introduction

Single-molecule magnets (SMMs) are open-shell metal complexes exhibiting slow relaxation of the magnetization and, as a result, magnetic hysteresis and remnant magnetization when the polarizing field is eliminated below the so-called blocking temperature (T_B).[1] In addition to these classical properties, SMMs show quantum properties such as quantum tunneling of the magnetization (QTM), quantum coherence and quantum oscillations. This association of classical and quantum properties makes this subclass of materials good candidates for potential technological applications such as high-density data storage, quantum sensing, quantum simu-

---

[a] *Departamento de Química Inorgánica, Facultad de Ciencias, Universidad de Granada, 18071 Granada, Spain. E-mail: ecolacio@ugr.es*
[b] *Departamento de Química Física y Analítica, Facultad de Ciencias Experimentales, Universidad de Jaén, Campus Las Lagunillas, 23071 Jaén, Spain*
[c] *Sorbonne Université Institut Parisien de Chimie Moléculaire, CNRS UMR 8232 4 place Jussieu 75252, Paris cedex 5, France*
[d] *National High Magnetic Field Laboratory, Florida State University, Tallahassee, Florida 32310, USA*

† Electronic supplementary information (ESI) available. CCDC 2334787–2334790. For ESI and crystallographic data in CIF or other electronic format see DOI: https://doi.org/10.1039/d4dt00622d

lation, and ultimately quantum computing.[1,2] The SMMs' behavior mainly depends on the magnetic anisotropy, which arises from the combined action of spin–orbit coupling (SOC) and ligand field effects. Therefore, it is not surprising that the best SMM properties have been observed for metal complexes containing very anisotropic lanthanide ions, particularly Dy^{III}. It is worth noting that, among these systems, those of mononuclear nature, also called single-ion magnets (SIMs), exhibiting large axial (easy-axis) anisotropy with negligible rhombicity terms, have been shown to be very efficient as SMMs with the U_{eff} (effective energy barrier for magnetization reversal) and T_B as high as 1540 cm^{-1} and 80 K, respectively.[3] These outstanding SIM properties have been achieved because in these mononuclear complexes the magnetic anisotropy can be deliberately regulated by playing with the geometry and electronic nature of the metal ion and the crystal field splitting, which ultimately depends on the electronic and steric effects of the ligands. Among transition metal complexes, some mononuclear linear, tetrahedral and trigonal prismatic Co^{II}-containing complexes with strong easy-axis anisotropy have also shown to be quite efficient SIMs with U_{eff} and T_B up to 450 cm^{-1} and 5 K, respectively.[4] Moreover, some of them are air stable, opening the door toward their incorporation in devices.

In this context, we, and others, have recently reported Co^{II} trigonal prismatic complexes with N_6-tripodal ligands exhibiting strong easy-axis anisotropy, and in some cases, slow relaxation of the magnetization at zero-field and a pinched at the waist hysteresis loop at 2 K.[5] Moreover, experimental and theoretical studies on these compounds established that the easy-axis anisotropy increases linearly as the distortion from TPR-6 to OC-6 decreases with a concomitant increase of the relaxation times.[5f,o,p] In other words, when the geometry becomes closer to the ideal TPR-6, the SIM properties improve. Moreover, some of the authors have recently shown that the large easy-axis anisotropy of trigonal prismatic Co^{II} ions in a Co_3 complex is mandatory, together with the collinearity of the anisotropy axes and magnetic exchange, for observing SMM behaviour at zero field with pinched at the waist hysteresis at 2 K.[6]

As a continuation of this work, we report here the synthesis, X-ray crystal structure, dc and ac magnetic properties and HFEPR and FIRMS spectroscopic studies of four new Co^{II} complexes with the Schiff base N_6-tripodal ligands tris(2-quinolylhydrazonyl)phosphorylsulfide, $(S)P[N(Me)N{=}C(H)(2\text{-}Q)]_3$ (**L**) and tris(1-isoquinolyl hydrazonyl)phosphorylsulfide, $(S)P[N(Me)N{=}C(H)(1\text{-}ISOQ)]_3$ (**L1**) (see Scheme 1) of formula $[Co(\mathbf{L})(SCN)_2(CH_3OH)_{0.5}(H_2O)_{0.5}]\cdot1.5H_2O\cdot0.75CH_3OH$ (**1**), $[Co(\mathbf{L1})Cl_2]\cdot H_2O\cdot2CH_3CN$ (**2**), $[Co(\mathbf{L1})(SCN)_2]\cdot1.5H_2O\cdot CH_3OH$ (**3**) and $[Co(\mathbf{L1})]ClO_4\cdot2CH_3OH$ (**4**).

The aim of this study is threefold: (i) to analyze how the use of bulky bicyclic aromatic moieties such as quinolyl and isoquinolyl modify the geometry of the CoN_6 coordination sphere and, therefore, the magnitude of the magnetic anisotropy regarding previously reported analogous trigonal prismatic Co^{II} complexes; we expect that the presence of bulky groups leads to a more distorted trigonal prismatic geometry and, then, to a decrease in the easy-axis magnetic anisotropy and to worse SIM properties; (ii) to study how the coordination in axial positions of the Co^{II} ion of two π-donor ligands (chloride or κ-N-thiocyanato), giving rise to a distorted octahedral CoN_4X_2 (Cl^- or SCN^-) coordination sphere, modifies the magnitude of the magnetic anisotropy compared with previously reported analogous complexes, and (iii) to analyze how the magnetic relaxation dynamics is affected when the size of the molecule increases.

Experimental

Synthetic procedures

General procedures. All reactions were conducted in oven-dried glassware in aerobic conditions and the analytical reagents were purchased from commercial sources and used without further purification. The precursor tris(methyl-

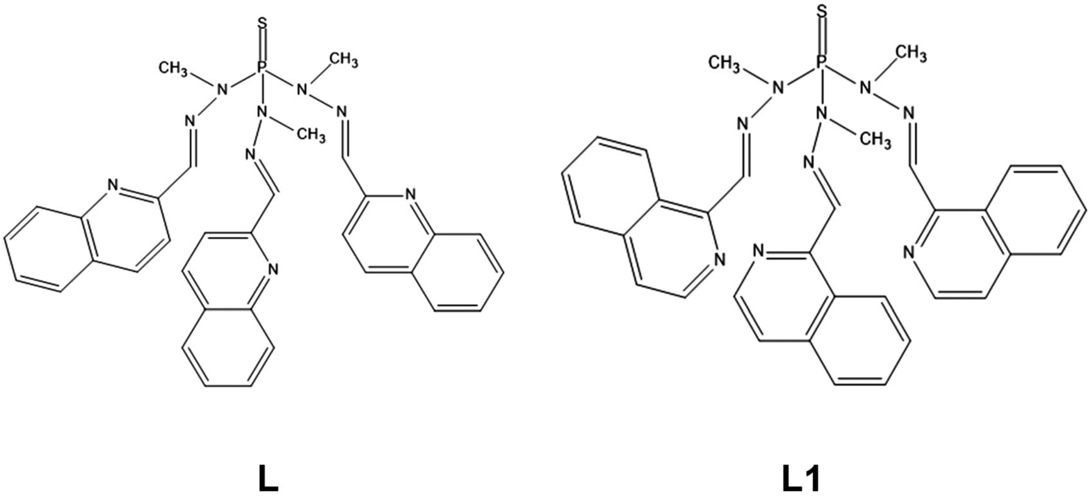

Scheme 1 Structures of the **L** and **L1** ligands.

hidrazido)phosphorylsulfide was prepared according to a previously described procedure.[7]

Synthesis of ligand (S)P[N(Me)N═C(H)(2-Q)]$_3$ (L). Tris(methylhidrazido)phosphorylsulfide (0.45 g, 2.25 mmol) and 2-quinolinecarboxaldehyde (1.06 g, 6.75 mmol) were dissolved in 40 mL of methanol. Afterwards, a few drops of acetic acid were added, and the mixture was refluxed for 21 hours and stirred at room temperature for 24 hours more. Then, the mixture was evaporated to dryness and the resulting yellow oil was recrystallised in chloroform. The solid formed was filtered off and dried in a vacuum. Yield: 47%. Anal. Calc. for $C_{33}H_{30}N_9PS$: C, 64.38; H, 4.91; N, 20.47: S, 5.21. Found: C, 63.97; H, 4.49; N, 20.68; S, 5.35. IR (cm^{-1}): 3100–2800, ν(CH); 1600–1400, ν(C═C and C═N) and 950 ν(P═S). ^{1}H NMR (CDCl$_3$, ppm): 8.05 (d, H_{ql}), 8.0 (s, H_{imine}), 7.78 (d, H_{ql}), 7.7 (m, H_{ql}), 7.6 (dd, H_{ql}), 7.45 (m, H_{ql}), 3.5 (s, H_{methyl}).

Synthesis of ligand (S)P[N(Me)N═C(H)(1-ISOQ)]$_3$ (L1). In 40 mL of methanol were dissolved tris(methylhidrazido)phosphorylsulfide (0.21 g, 1.06 mmol) and isoquinolinecarboxaldehyde (0.5 g, 3.18 mmol) together with a few drops of acetic acid. The mixture was refluxed for seven hours and then stirred at room temperature for 16 hours more. The precipitated ligand was filtered off and dried in a vacuum. Yield: 31%. Anal. Calc. for $C_{33}H_{30}N_9PS$: C, 64.38; H, 4.91; N, 20.47: S, 5.21. Found: C, 64.17; H, 5.35; N, 20.48; S, 5.26. IR (cm^{-1}): 3000–2800, ν(CH); 1600–1400, ν(C═C and C═N) and 900 ν(P═S). ^{1}H NMR (CDCl$_3$, ppm): 9.25 (d, H_{iql}), 8.5 (d, H_{iql}), 8.3 (s, H_{imine}), 7.65 (d, H_{iql}), 7.5 (d, H_{iql}), 7.4 (m, H_{iql}), 7.05 (m, H_{iql}), 3.5 (s, H_{methyl}).

Synthesis of [Co(L)(SCN)$_2$(CH$_3$OH)$_{0.5}$(H$_2$O)$_{0.5}$]·1.5H$_2$O·0.75 CH$_3$OH (1). A solution of Co(SCN)$_2$ (15 mg, 0.08 mmol) in 10 mL of MeOH was added with continuous stirring to a solution of the ligand **L** (50 mg, 0.08 mmol) in 10 ml of MeOH. The resulting red solution was stirred for five minutes and then was kept at room temperature. After several days, X-ray-quality red crystals of **1** were obtained by slow evaporation of the solution. Yield: 8%. Anal. Calc. for $C_{36.2}H_{39}CoN_{11}O_{3.2}PS_3$: C, 50.23; H, 4.53; N, 17.77: S, 11.10. Found: C, 50.36; H, 4.58; N, 17.81; S, 11.01. IR (cm^{-1}): 2066, ν(SCN); 1600–1400, ν(C═C and C═N) and 950 ν(P═S). ESI-MS (Da): *m*/*z* 732.09, [Co(**L**)(SCN)]$^+$; *m*/*z* 616.18, L$^+$; *m*/*z* 369.06, [Co(**L1**)(CH$_3$OH)$_2$]$^{2+}$.

Synthesis of [Co(L1)Cl$_2$]·H$_2$O·2CH$_3$CN (2). A solution of CoCl$_2$·6H$_2$O (12 mg, 0.049 mmol) in 10 ml of acetonitrile was added with continuous stirring to a solution of the ligand **L1** (30 mg, 0.049 mmol) in acetonitrile (10 ml). The solution was stirred for five minutes and then allowed to stand at room temperature. X-ray-quality green crystals of **2** were obtained after several days. Yield: 24%. Anal. Calc. for $C_{37}H_{38}Cl_2CoN_{11}OPS$: C, 52.55; H, 4.53; N, 18.22: S, 3.79. Found: C, 52.66; H, 4.89; N, 18.38; S, 3.97. IR (cm^{-1}): 1600–1400, ν(C═C and C═N) and 900 ν(P═S).

Synthesis of [Co(L1)(SCN)$_2$]·1.5H$_2$O·CH$_3$OH (3). This compound was prepared following the same methodology as for compound **2** but using Co(SCN)$_2$·6H$_2$O (9 mg, 0.049 mmol) and methanol instead of CoCl$_2$·6H$_2$O and acetonitrile. After a few days, well-formed crystals of **3** were obtained by slow evaporation of the solution. Yield: 25%. Anal. Calc. for $C_{36}H_{37}CoN_{11}O_{2.5}PS_3$: C, 50.88; H, 4.39; N, 18.13: S, 11.32. Found: C, 50.71; H, 4.64; N, 17.93; S, 11.10. IR (cm^{-1}): 2059, ν(SCN); 1600–1400, ν(C═C and C═N) and 900 ν(P═S).

Synthesis of [Co(L1)](ClO$_4$)$_2$·2CH$_3$OH (4). This compound was prepared following the same method as for compound **3** but using Co(ClO$_4$)$_2$·6H$_2$O (19 mg, 0.049 mmol) instead of Co(SCN)$_2$·6H$_2$O. The resulting solution was left at room temperature for slow evaporation and after a few days, suitable dark red crystals for X-ray diffraction were obtained. Yield: 22%. Anal. Calc. for $C_{35}H_{38}Cl_2CoN_9O_{10}PS$: C, 44.84; H, 4.09; N, 13.44: S, 3.42. Found: C, 45.06; H, 4.29; N, 13.56; S, 3.30. IR (cm^{-1}): 1600–1400, ν(C═C and C═N); 1075, ν(Cl–O) and 900 ν(P═S). ESI-MS (Da): *m*/*z* 773.09, [Co(**L1**)]$^{2+}$(ClO$_4$); *m*/*z* 337.07, [Co(**L1**)]$^{2+}$.

Synthesis of the diluted sample 4′. 10 mL of a methanolic solution containing Co(ClO$_4$)$_2$·6H$_2$O (3.3 mg, 0.008 mmol) and Zn(ClO$_4$)$_2$·6H$_2$O (32.9 mg, 0.080 mmol) was added with continuous stirring to a solution of the ligand **L1** (59.7 mg, 0.088 mmol) in 10 mL of methanol. After 15 minutes a precipitate formed, which was filtered off and dried in air. Yield: 31%. Anal. Calc. for $C_{35}H_{38}Cl_2Co_{0.1}Zn_{0.9}N_9O_{10}PS$: C, 44.56; H, 4.06; N, 13.36: S, 3.40. Found: C, 44.43; H, 4.03; N, 13.36; S, 3.66. IR (cm^{-1}): 1600–1400, ν(C═C and C═N); 1088, ν(Cl–O) and 900 ν(P═S). ESI-MS (Da): *m*/*z* 780.07, [Zn(**L1**)]$^{2+}$(ClO$_4$); *m*/*z* 340.5, [Zn(**L1**)]$^{2+}$.

It is worth noting that all attempts to obtain the diluted version of compounds **1–3** were unsuccessful.

Physical measurements

Elemental analyses were performed on a Fisons-Carlo Erba analyser model EA 1108 and ^{1}H-NMR spectra on a 400 Hz "VARIAN DIRECT DRIVE" spectrometer at the "Centro de Instrumentación Científica" (University of Granada). IR spectra were recorded on a Bruker Tensor 27 spectrophotometer by using ATR detection. The X-ray powder diffraction (XRPD) spectra were registered on a (2θ) Bruker D2-PHASER using CuKα (λ = 1.5418 Å) radiation and LYNXEYE detector, from 5 to 50° (2θ) at a scanning rate of 0.5° 2θ/min (Fig. S1†).

Variable-temperature (2–300 K) magnetic susceptibility measurements were carried out on polycrystalline samples under an applied field of 1000 Oe using DynaCool PPMS-9 physical measurement equipment (**1**, **4′**) or a Quantum Design SQUID MPMS XL-5 (**4**) or XL-7 (**2**, **3**) device. Alternating-current (ac) susceptibility measurements under different applied static fields in the temperature range 2–15 K were performed in PPMS-9 physical measurement equipment in the 50–10 000 Hz frequency range, using an oscillating field H_{ac} = 10 Oe (**2**, **3**) or H_{ac} = 5 Oe (**4′**). The ac measurements of complex **4** were recorded using a Quantum Design SQUID MPMS XL-5 device under an oscillating ac field of 4 Oe and ac frequencies in the 1–1500 Hz range. The magnetic susceptibility values were corrected for the diamagnetism of the molecular constituents and sample holder.

Far-infrared magnetic spectroscopy (FIRMS, also known as frequency-domain THz EPR spectroscopy)[8] experiments of compounds **2–4** (no clear magnetic peaks were observed in the spectrum of **1**) were performed at the National High Magnetic Field Laboratory using a Bruker Vertex 80v FT-IR spectrometer coupled with a 17 T vertical-bore superconducting magnet in a Voigt configuration (light propagation perpendicular to the external magnetic field). The experimental setup employs broad band terahertz radiation emitted by a mercury arc lamp. The radiation transmitted through the sample was detected by a composite silicon bolometer (Infrared Laboratories) mounted at the end of the quasioptical transmission line. Both the sample and bolometer were cooled by low-pressure helium gas to the temperature of 5 K. The intensity spectra of the microcrystalline powder sample (~2 mg) bonded by n-eicosane were measured in the spectral region between 14 and 730 cm^{-1} (0.42–22 THz) with an instrumental resolution of 0.3 cm^{-1} (9 GHz). To discern the magnetic absorption, the transmission spectrum at each magnetic field was divided by the reference spectrum, which is calculated as the average spectrum for all magnetic fields after removing outlier points at each frequency. Such normalized spectra are only sensitive to tiny transmission changes induced by the magnetic field and exclude a strong nonmagnetic contribution due to vibrational absorptions and an instrumental function. All the data analysis routine was implemented by in-house-written MATLAB code based on the EPR simulation software package EasySpin.[9]

High-frequency and high-field EPR (HFEPR) spectra of compounds **2–4** were recorded at the National High Magnetic Field Laboratory in a 4.5–10 K temperature range on polycrystalline samples (20–25 mg), using a homodyne spectrometer at the EMR facility associated with a 15/17-T superconducting magnet and a frequency range from 52 to 426 GHz.[10] Detection was provided with an InSb hot electron bolometer (QMC Ltd, Cardiff, UK). The magnetic field was modulated at 50 kHz for detection purposes. A Stanford Research Systems SR830 lock-in amplifier converted the modulated signal to dc voltage.

Single-crystal structure determinations

Suitable crystals of **1–4** were mounted on a glass fibre and used for data collection. X-ray diffraction data were collected at 100 K using a Bruker D8 Venture diffractometer (MoKα radiation, $\lambda = 0.71073$ Å) fitted with a PHOTON 100 detector. Unit-cell parameters were determined and refined on all the observed reflections using APEX2 software.[11] Correction for Lorentz polarization and absorption was applied by the SAINT[12] and SADABS[13] programs, respectively.

The structures were solved using SHELXS (**2**, **3**)[14] or SHELXT (**1**, **4**)[15] and refined by the full-matrix least-squares method on F2 using the SHELXL-2014/2018[16] and OLEX2 programs.[17]

The data collected for compound **1** were of very bad quality. For that reason, a low value of resolution was chosen for data integration as the reflections that appear below this resolution were very weak. In **1**, the two quinoline molecules that remain free were generated from the quinoline molecule that is coordinated to the Co^{II} ion. In addition, the uncoordinated quinolines were heavily disordered, and the anisotropic model could not be applied, so the atoms were considered isotropically. One SCN anion was disordered and could be modelled satisfactorily. The oxygen atom coordinated to Co^{II} belongs half time to a water molecule and half time to a methanol molecule. Moreover, in the solvent molecules, the hydrogen atoms bonded to water and methanol molecules could not be reliably positioned and this causes checkCIF alerts concerning the chemical formula. Therefore, all the alerts from the structure of **1** are, mainly, due to the bad quality of the collected data. In compound **3**, one of the isoquinoline molecules and the oxygen atom from the methanol and water solvent molecules are disordered, and the disorder model was satisfactory. However, the hydrogen atoms associated with the solvent water molecule could not be directly located from difference Fourier maps. For this reason, the calculated and reported SumFormula differs. In addition, one perchlorate anion of compound **4** is also heavily disordered over two positions. It could be modelled satisfactorily but the oxygen atoms were refined isotropically. In all cases, the hydrogen atom positions were calculated and isotropically refined as riding models to their parent atoms.

A summary of selected data collection and refinement parameters can be found in the ESI (Table S1†) and CCDC 2334787–2334790.†

Computational methodology

Calculations were carried out from the crystallographic structures using the cif files. The electronic structure and magnetic properties have been computed using state-averaged complete active space self-consistent field calculations (SA-CASSCF (7,5)),[18] followed by the N-electron valence second-order perturbation theory (NEVPT2) method[19] with the def2-TZVPP basis set,[20] including the auxiliary basis sets for correlation and Coulomb fitting for all the atoms. All calculations were done with the ORCA 5.0.2 quantum chemistry program package.[21] Spin Hamiltonian parameters (D, E and g-tensor) were computed using the effective Hamiltonian $S = 3/2$. In this case, spin–orbit effects were included using the quasi-degenerate perturbation theory (QDPT).[22,23] The employed active space includes seven electrons in five 3d-orbitals of Co^{II} CAS (7,5). We have included all 10 states for the $2S + 1 = 4$ (quartet) states arising from the 4F and 4P terms of Co^{II}, and all 40 states for the respective $2S + 1 = 2$ (duplet) states arising from the 2P, 2D (twice), 2F, 2G and 2H terms of the Co^{II} ion. ORCA produces two sets of results: CASSCF and NEVPT2. The splitting of d-orbitals due to the ligand field has been computed with the *ab initio* ligand field theory (AILFT)[24] module implemented in the ORCA program package.

Results and discussion

The new ligands were obtained by condensation between tris(methylhydrazine)phosphorylsulfide and either 2-quinolinecarboxaldehyde or isoquinoline-1-carbaldehyde in methanol containing some drops of acetic acid for catalyzing the reaction. The ligand **L** reacts with $Co(SCN)_2·6H_2O$ in a 1 : 1 molar ratio and using methanol as solvent, leading to the compound (**1**). All attempts to obtain other complexes with this ligand using different Co^{II} salts (with coordinating and non-coordinating anions Cl^-, Br^-, BF_4^-, ClO_4^-, NO_3^-), Co^{II}/**L** ratios (2/1, 1/1 and 1/2) and solvents (EtOH, CH_3CN, MeOH and DMF) were unsuccessful. It is worth noting that in **1** the **L** ligand does not coordinate to Co^{II} in a tripodal fashion, but as a S,N,N-tridentate ligand, so that only one arm of **L** coordinates to the Co^{II} ion (see below). The N_6-tripodal coordination mode of this ligand could promote a strong steric hindrance between the bulky quinolyl aromatic bicyclic moieties of the three arms of the ligand, because they would be orientated toward the inner part of the complex and placed close to each other. This is the reason why the Co^{II} complexes with the ligand **L** coordinated in a N_6-tripodal fashion and even with only two arms coordinated to the Co^{II} would be unstable. In view of this, we designed **L1**, which when it coordinates to the Co^{II} either in an N_6-tripodal manner or in a bis-bidentate fashion (when only two arms of the ligand are coordinated to the Co^{II} ion) has the isoquinolyl moieties oriented toward the outer part of the complex. Therefore, the steric hindrance significantly diminishes and complexes where the ligand presents these coordination modes could be formed. In fact, the reaction of **L1** with different Co^{II} salts led to the formation in a good yield of the crystalline complexes **2–4**. It is worth noting that the reaction between **L1** and Co^{II} salt-containing medium to strong coordinating anions, such as chloride or thiocyanate, using different Co^{II}/ligand molar ratio and solvents, in no case led to the N_6-coordinated cationic complexes $[Co(\mathbf{L1})]X_2$ ($X = Cl^-$, SCN^-), but to neutral compounds $[Co(\mathbf{L1})X_2]$. In these latter ones, the ligand shows a bisbidentate coordination mode and the corresponding anions coordinate in *trans* positions. The formation of the complex $[Co(\mathbf{L1})Cl_2]$ (**2**) seems to indicate that the coordination ion of two chloride anions to the Co^{II} instead of two N-donor atoms belonging to one arm of the **L1** ligand is either faster and/or thermodynamically more favorable with the **L1** ligand than with other less bulky closely related N_6-tripodal ligands.[5o,p] These latter coordinate to the Co^{II} in an N6-tripodal mode leading to complexes of formula $[Co(L')][CoCl_4]$ (L′ is the N6-tripodal ligand bearing pyridine or imidazole moieties instead of isoquinoline). However, the reaction of $Co(ClO_4)_2$ with **L1** led to complex **4**, where the ligand was able to coordinate the three arms to the Co^{II} ion, due to the poor coordination ability of the perchlorate anion.

Crystal structures

Compound **1** crystallizes in the triclinic space group $P\bar{1}$. Fig. 1 shows the molecular structure of this complex, which is formed by neutral mononuclear units $[Co(\mathbf{L})(SCN)_2(MeOH)_{0.5}(H_2O)_{0.5}]$ and three quarters of a methanol and one and a half water molecules of crystallization. Selected bond distances and angles are shown in Table S2.†

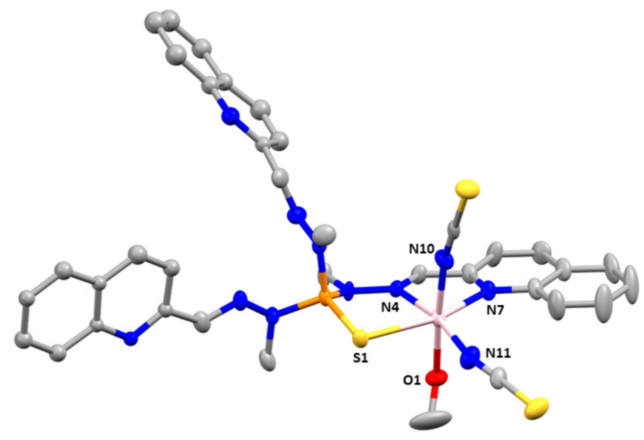

Fig. 1 Molecular structure and numbering scheme of compound **1**. Thermal ellipsoids at 50% probability level are shown. The hydrogen atoms and solvent molecules have been omitted for clarity. Only one position of disordered free quinoline molecules and thiocyanate anion is shown. Colour code: pink Co, orange P, blue N, silver C, yellow S, red O.

Within the mononuclear unit, only one arm of the tripodal **L** ligand is coordinated to Co^{II}, the other two arms remaining free. The ligand coordinates to the Co^{II} ion in a tridentate chelate coordination mode through the nitrogen atoms of the azomethine group, the quinoline moiety and the sulphur atom of the P═S group. The nitrogen atoms of two thiocyanate anions are in *cis* positions and the oxygen atom of a water/methanol molecule completes the distorted octahedral CoN_4OS coordination geometry of the Co^{II} ion. It is worth noting that, as far as we know, this is the first time that this coordination mode has been observed for this type of tripodal ligand. Although a complex with a tripodal ligand like **L**, where the P═S is S-coordinated to an Ag^I ion, was certainly reported, the ligand does not act as a N,N,S-tridentate ligand with two free arms as in **1**, but as a $S(NN)_2$ pentadentate bridging ligand with only a free arm and the sulphur atom acting as bridge between two Ag^I ions.[25]

As previously observed for Co^{II} complexes with this type of tripodal ligand bearing two N-coordinated thiocyanate ligands,[5o] the $Co–N_{SCN}$ bond distances seem to be shorter than the $Co–N_L$ counterparts. Moreover, as expected, the Co–S bond distance appears to be the longest one.

As mentioned above (single-crystal structure determinations), the data collected for **1** were of very bad quality. In consequence, it is not possible to describe properly the intermolecular interactions. However, it seems that there exist weak intermolecular π–π interactions between the quinoline molecules pertaining to the free arms of two different complexes, which lead to a shortest intermolecular Co⋯Co distance of less than 7.5 Å. This distance suggests that the Co^{II} molecules are not well isolated in the crystal lattice.

Compounds **2** and **3** crystallize in the monoclinic space group $C2/c$. The structures consist of neutral mononuclear molecules $[Co(\mathbf{L1})Cl_2]$ or $[Co(\mathbf{L1})(SCN)_2]$ together with two acetonitrile and one water solvent molecule for **2** and one

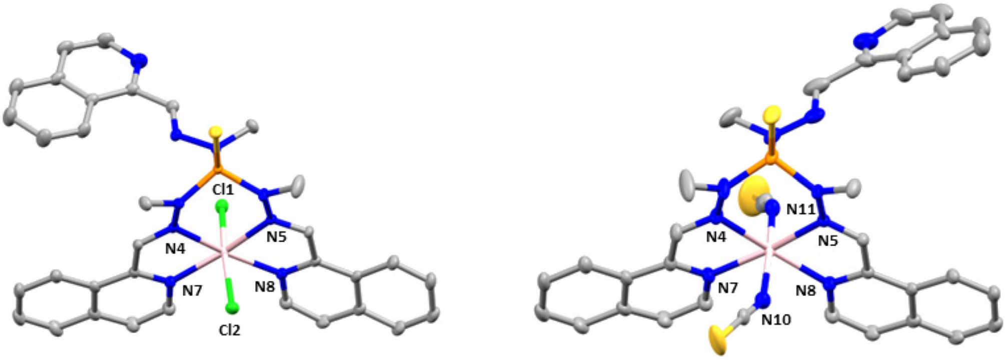

Fig. 2 Molecular structures of **2** (left) and **3** (right). Thermal ellipsoids at 50% probability level are shown. In **3**, only one position of the disordered isoquinoline molecule is shown. Hydrogen atoms and solvent molecules are omitted for clarity. Colour code: pink Co, orange P, blue N, silver C, yellow S, green Cl.

methanol and one and a half water molecules in the case of **3** (Fig. 2).

In these complexes, the Co^{II} ion is coordinated by two chloride anions (or two thiocyanate ligands for **3**) and two arms of the **L1** ligand, the third one remaining uncoordinated. In this arrangement, the Co^{II} exhibits a distorted octahedral coordination sphere (CoN_4Cl_6 for **2** and CoN_6 for **3**), where the two Cl^- anions in **2** (or two nitrogen atoms from two SCN^- anions in **3**) are in *trans* positions and two isoquinoline and two imine nitrogen atoms belonging to two of the three arms of the tripodal ligand are in the equatorial plane. Selected bond distances and angles for **2** and **3** are shown in Table S3.†

As can be observed the Co–Cl bond distances in **2** are notably larger than the Co–N ones, whereas the Co–N_{SCN} bond distances, as observed in **1**, are the shortest ones in the coordination sphere of **3**. With respect to the Co–N bond distances involving donor atoms from the ligand, those belonging to the isoquinoline moiety are slightly smaller than the Co–N bond distances corresponding to the azomethine groups. The shortest intermolecular Co⋯Co distance for **2** is 8.300 Å and for **3** is 8.301 Å.

Finally, there are π–π intermolecular interactions between the coordinated isoquinoline rings with a centroid–centroid distance of 3.900 Å for **2** and 3.693 Å for **3** and between the isoquinoline rings that remain uncoordinated (4.492 Å for **2** and 4.441 Å for **3**). Additionally, in **3** there exist hydrogen bond interactions between solvent water molecules (O1 and O3) with a donor–acceptor distance of 2.872 Å and between the oxygen atom pertaining to a water solvent molecule and the nitrogen atom belonging to the isoquinoline ring with a donor–acceptor distance of 2.910 Å.

Complex **4** crystallizes in the monoclinic space group $P2_1/n$. The structure consists of cationic mononuclear units $[Co(\mathbf{L1})]^{2+}$ together with two perchlorate anions and two solvent methanol molecules (Fig. 3).

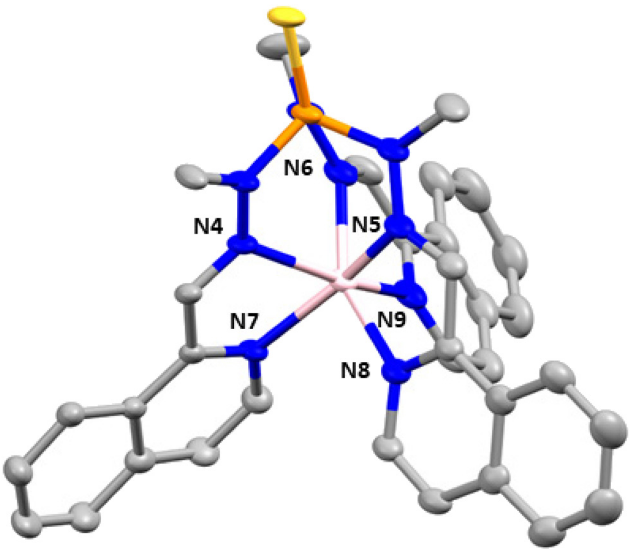

Fig. 3 Crystal structure of compound **4**. Thermal ellipsoids at 50% probability level are shown. The hydrogen atoms, perchlorate anions and solvent molecules are omitted for clarity. Colour code: pink Co, orange P, blue N, silver C, yellow S.

Within the mononuclear unit, the Co^{II} ion presents a CoN_6 coordination sphere formed by six nitrogen atoms belonging to the three arms of the ligand that lead to an intermediate geometry between octahedral and trigonal prism, but closer to trigonal prism. Although the Co–N bond distances belonging to the nitrogen atoms of the azomethine group and the nitrogen atoms of the isoquinoline moieties are similar, those involving the isoquinoline nitrogen atoms are slightly larger than the former ones, in opposite direction to that observed in compounds **2** and **3**. Moreover, in general, the Co–N distances in compounds **2** and **3** are larger than those in compound **4**. The selected bond distances and angles are shown in Table S4.† The shortest intermolecular Co⋯Co distance between molecules is 10.203 Å, indicating that the mononuclear units are well isolated in the structure.

Finally, there are intermolecular hydrogen bond interactions between the methanol molecules and perchlorate anions with distances in the range of 2.782–3.022 Å. In addition, the structure shows π–π interactions between the iso-quinolines of neighboring molecules, with a centroid–centroid distance of 3.847 Å.

In all the compounds, the coordination geometry adopted by the Co^{II} ion has been evaluated through SHAPE software, which is based on the continuous shape measurements method (CShMs).[26a] The coordination sphere of the compounds **1–4** is found between the ideal octahedral (OC-6) and trigonal prism (TRP-6) structures (Table S5†).

In the case of complexes **1–3**, where the ligand is not coordinated to the Co^{II} ion using its three arms, the S(OC-6) values are found in the 1.5–2.5 range, while the values of S(TPR-6) are found in an 11–12 range. This fact indicates that the coordination geometry of the Co^{II} ion for these three compounds, though axially distorted, is close to octahedral. These values compare well with those calculated for the complex $[Co(L3)(SCN)_2]$ **11**. In the case of compound **4**, in which the three arms of the ligand are coordinated to Co^{II} ion, the values of S(OC-6) and S(TPR-6) are 5.602 and 4.322, respectively, thus indicating that the coordination geometry adopted by the Co^{II} ion is intermediate between an octahedron and a trigonal prism, but closer to the latter one. Moreover, the deviation with respect to the ideal Bailar path for the interconversion between the OC-6 and TPR-6 ideal geometries (Fig. 4) is very small (6.4%). The distortion of the geometry along the OC6 ↔ TPR6 pathway was also calculated using the recently proposed structural parameter (τ_6).[26b] This geometry index is zero for the ideal OC-6 geometry and 1 for the ideal TPR6 shape (see Table S5†). The calculated τ_6 values correlates well with the S values extracted with the continuous shape measures, confirming that the coordination environment of compounds **1–3** is close to the OC-6 geometry, whereas compound **4** presents a coordination sphere that is slightly closer to TPR-6 than to OC-6.

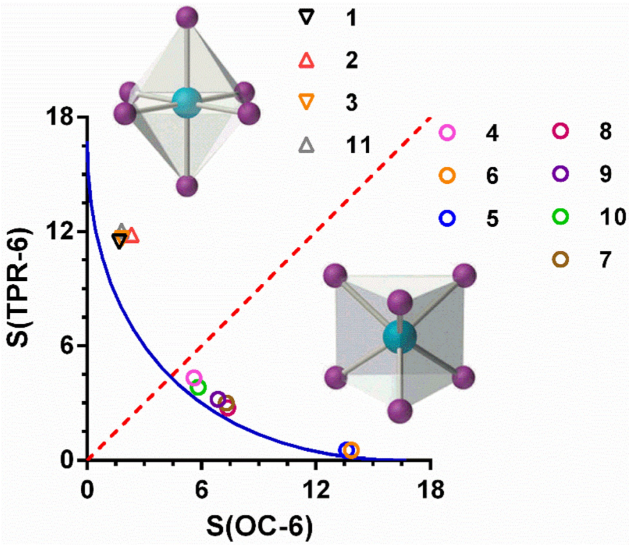

Fig. 4 Octahedron-trigonal prism shape map showing the Bailar pathway (blue line) and the experimental data (circles) for compounds 1–11 (see text). The dotted red line separates complexes with TPR-6 and OC-6 geometries.

Compared with other similar compounds already reported by some of us, in which the tripodal ligand also presents a CoN_6 coordination sphere, compound **4** possesses the most intermediate coordination geometry between OC-6 and TPR-6 (Fig. 4). Among these compounds, those containing tripodal ligands with methylimidazole moieties in the arms (L2), $[Co(L2)]X_2$ ($X = ClO_4^-$, **5** and BF_4^-, **6**), exhibit coordination spheres very close to the ideal TPR-6 geometry and continuous shape measures S(TPR-6) of 0.533 and 0.486 for **5** and **6**, respectively. However, for the compounds containing ligand with pyridine moieties in the arms (L3), $[Co(L3)]X_2$ ($X = ClO_4^-$ **7**, BF_4^- **8**, $ZnCl_4^{2-}$ **9**, $CoCl_4^{2-}$ **10**), the CoN_6 coordination environment is less distorted than **4** but more than **5** and **6** with S(TPR-6) values of 3.002 and 2.759, 3.196 and 3.839 for **7**, **8**, **9** and **10**, respectively.

Magnetic properties

The magnetic properties of polycrystalline samples of complexes **1–4** were collected in the 2–300 K temperature range under an applied magnetic field of 1000 Oe. They are given in the form $\chi_M T$ *vs.* T (χ_M being the molar magnetic susceptibility) in Fig. 5. The $\chi_M T$ values at room temperature for **1–4** of 2.72, 2.80, 2.72 and 2.87 cm^3 mol^{-1} K, respectively, are much higher than the spin-only value (1.875 cm^3 mol^{-1} K) for one isolated isotropic Co^{II} ion with $g = 2$ and $S = 3/2$, which points to an unquenched orbital angular momentum of the Co^{II} ions. As the temperature is lowered, the $\chi_M T$ product decreases first slightly from room temperature to about 100 K and then in a sharper manner to reach minimum values at 2 K of 1.66, 1.60, 1.64 and 2.14 cm^3 mol^{-1} K for **1–4**, respectively. This behavior is mainly due to the depopulation of the Kramers doublets arising from the spin–orbit coupling (SOC) effects, which ultimately are responsible for the magnetic anisotropy.

The field dependence of the magnetization for **1–4** in the 2–7 K temperature range and magnetic fields ranging from 0 to 7 T are given in the insets of Fig. 5. The magnetization values at 2 K and under the maximum applied field of 7 T (5 T in the case of **4**) of 2.10, 2.2, 2.18 and 2.10 $N\beta$ for **1–4**, respectively, are far away from the theoretical saturation value of $3N\beta$ expected for an isolated Co^{II} ion with $g = 2$ and $S = 3/2$, thus confirming the existence of significant magnetic anisotropy in these complexes. The M *vs.* H and M *vs.* H/T isotherms for compounds **1–4** are shown in Fig. S2–S5.† The latter show only a slight dependence on the temperature for complexes **1–3**, whereas for **4** the curves virtually superimpose in a single manner, thus suggesting that the energy separation between the ground and first excited Kramers doublets could be very large for these compounds, particularly for complex **4**.

From the results of the theoretical *ab initio* calculations for **1–4** (see below) and using the criterion recently proposed by Boca *et al.*,[27] for quantitatively evaluating the rightness of the spin Hamiltonian theory (hereafter named zero field splitting Hamiltonian, ZFS, eqn (1)) in octahedral and axially distorted octahedral high spin Co^{II} complexes, we can conclude that the application of the ZFS model for analyzing the local magnetic

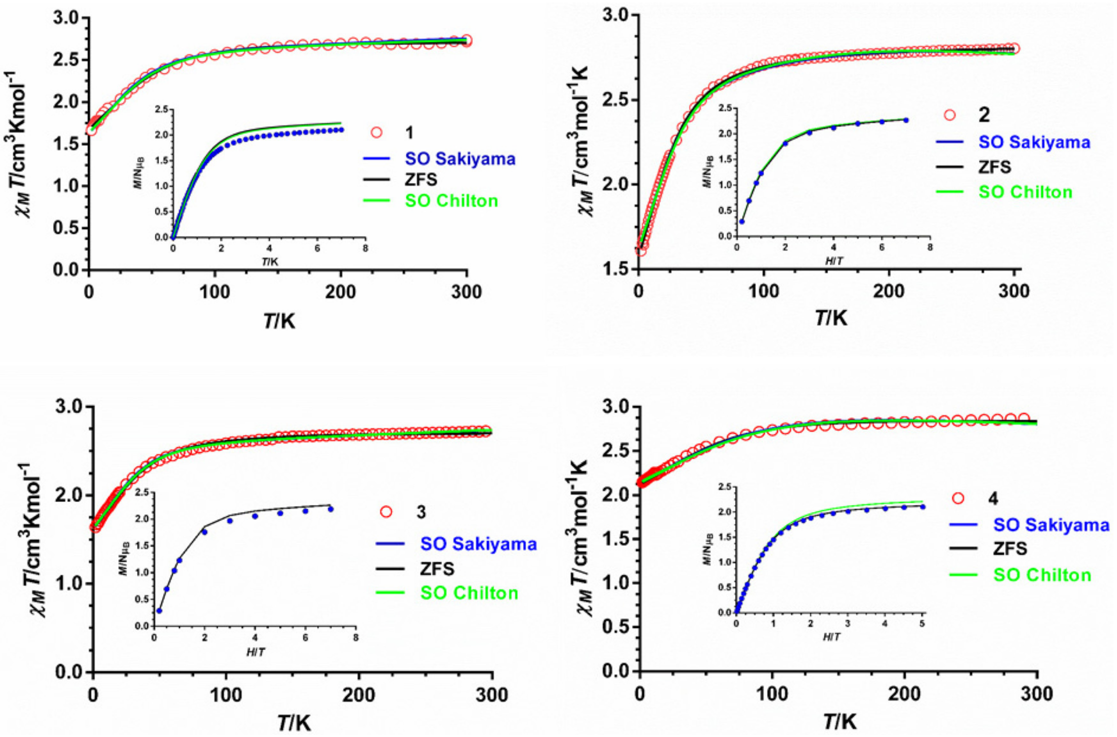

Fig. 5 Temperature dependence of $\chi_M T$ (red circles) and field dependence of the magnetization at 2 K (inset, blue circles). Solid lines represent the best fit to eqn (1) (black line), (2) (green line) and (3) (blue line) with the parameters indicated in Table 1.

anisotropy of the Co^{II} ions would be appropriate for complexes **1–3**. Nevertheless, the limitations of the phenomenological approach based on the ZFS Hamiltonian and the low accuracy of the magnetic measurements for determining the E and $|E/D|$ parameters prevent extracting very reliable ZFS parameters for complexes **1–3**, particularly the sign of D and the magnitude of E. Therefore, the D values extracted from the dc magnetic measurements should be considered with caution and, in any case, supported by other techniques.

On the other hand, the use of the ZFS Hamiltonian in the case of **4**, which exhibits a trigonal prismatic geometry and first order spin–orbit coupling, cannot be justified. In view of this, a Hamiltonian that explicitly considers this fact, like the Griffith–Figgis Hamiltonian (GF),[28] would be, in principle, more appropriate than the ZFS approach. The GF model exploits the T–P isomorphism that takes into consideration that the real orbital angular momentum for the $^4T_{1g}$ ground state in an ideal Oh geometry is equal to the orbital angular momentum of the ^4P free ion term multiplied by −3/2 and, therefore, the $^4T_{1g}$ is considered as having an effective orbital moment $L_{\text{eff}} = 1$. Although the GF model was developed for octahedral or axially distorted octahedral (square bipyramid) complexes, it has been also successfully applied to square-pyramidal distorted complexes.[29] In this case, the two lowest crystal-field terms derive from the splitting of the $^4T_{1g}$ term and, therefore, the T–P isomorphism could be applicable. However, for distorted trigonal prismatic complexes, where the lowest crystal-field terms arise from the ^4E ground term, this choice is more questionable. It should be noted at this point that, regardless of the inappropriateness of the ZFS model in the case of **4**, it has been widely applied for analyzing the magnetic anisotropy in trigonal prismatic Co^{II} complexes, since, as far as we know, there is no specific model for trigonal prismatic Co^{II} complexes accounting for unquenched orbital momentum. In view of the above considerations, the magnetic anisotropy parameters extracted from the ZFS and GF Hamiltonians should be taken with caution, as neither of these two approaches is fully appropriate for analyzing the magnetic data of **4**. Finally, although, as indicated above, the ZFS Hamiltonian is appropriate for analyzing the magnetic data of complexes **1–3**, we have also evaluated the magnetic data of these complexes, which possess a large contribution of the orbital angular momentum, using the GF model implemented in Chilton's PHI software[30a] (eqn (2)).

Thus, the magnetic susceptibility and magnetization data for **1–4** were simultaneously fitted with the ZFS, as well as with the GF phenomenological Hamiltonians using the PHI program.

The ZFS Hamiltonian is shown in eqn (1).

$$\hat{H} = D[\hat{S}_z{}^2 - S(S+1)/3] + E(\hat{S}_x{}^2 - \hat{S}_y{}^2) + \mu_B \sum_{i=x,y,z} g_i \vec{H}_i \hat{S}_i \quad (1)$$

where the first and second terms account for the axial magnetic anisotropy and the rhombic magnetic anisotropy, respectively, and the third term represents the Zeeman interaction.

The GF Hamiltonian is as follows:

$$\begin{aligned}\hat{H} = & -\sigma\lambda\hat{\mathbf{L}}\hat{\mathbf{S}} + \sigma^2 B_2^0\left(3\hat{\mathbf{L}}_z{}^2 - \hat{\mathbf{L}}^2\right) + \frac{B_2^2}{2}\sigma^2\left(\hat{\mathbf{L}}_x{}^2 - \hat{\mathbf{L}}_y{}^2\right) \\ & + \mu_B\left[-\sigma\hat{\mathbf{L}}_u + g_e\hat{\mathbf{S}}_u\right]\vec{H}_u \quad (u = x, y, z)\end{aligned} \tag{2}$$

This Hamiltonian operates on the ground $^4T_{1g}$ term of the octahedral high spin Co^{II} ion. The first term describes the interaction between the spin (S = 3/2) and orbital (L = 1) angular momenta through the spin–orbit coupling, where λ represents the spin–orbit coupling constant. The parameter σ represents a combined reduction factor, which comprises the isomorphism coefficient (−3/2) and the orbital-reduction parameter (κ) that considers the covalence effect and the mixing of the $^4T_{1g}$ (^4F) and $^4T_{1g}$ (^4P) terms (σ varies from −3/2 for a weak ligand field to −1 for a strong ligand field). The second and third terms represent the effect of the axial and rhombic crystal fields (B_2^0 and B_2^2 are the crystal field parameters).

The best fit parameters for compounds **1–4** using the ZFS and GF Hamiltonians are given in Table 1, whereas the corresponding curves are given in Fig. 5. It should be noted that the values extracted for Δ_{axial} with the GF Hamiltonian (eqn (2)) are very similar to those extracted with Sakiyama's software for distorted octahedral high-spin Co(II) complexes with axial symmetry (see Table 1), which uses the related GF Hamiltonian:[30b]

$$\begin{aligned}\hat{H} = & -3/2\kappa\hat{\mathbf{L}}\hat{\mathbf{S}} + \Delta_{\text{ax}}\left(\hat{\mathbf{L}}_z{}^2 - \frac{2}{3}\right) + \mu_B\left[-3/2\hat{\mathbf{L}}_u + g_e\hat{\mathbf{S}}_u\right] \\ & \vec{H}_u \quad (u = x, y, z)\end{aligned} \tag{3}$$

Table 1 Hamiltonian parameters extracted from the magnetic data using ZFS and GF models

Complex	**1**	**2**	**3**	**4**
Fitting to ZFS model eqn (1)				
D/cm^{-1}	55.0(6)	34.9(2)	33.2(3)	−80.9(1)
E/cm^{-1}	0 (fixed)	7(1)	10.18(6)	−0.02(1)
g_x,g_y	2.459(3)			2.245(1)
g_z	2.28(1)			2.756(1)
g_{iso}		2.437(1)	2.403(1)	
zJ'		−0.031(1)	−0.003(1)	
ΔE_1/cm^{-1}	110.1	73.9	75.2	161.8
Fitting to the GF model eqn (2)				
σ	−1.5 (fixed)	−1.238(4)	−1.50(1)	−1.29(1)
λ/cm^{-1}	−153(1)	−93.1(4)	−124.6(5)	−150.3(1)
B_2^0/cm^{-1}	175(1)	82.0(8)	150.3(5)	−334.3(2)
B_2^2/cm^{-1}	2.3(9)	1.9(9)	8(1)	−2.13(2)
Δ_{axial}	1181.0(1)	376.6(8)	1014.5(5)	−1668.9(3)
Δ_{rhombic}	2.6(9)	1.45(9)	9(1)	−1.77(2)
ΔE_1/cm^{-1} [a]	106.1	79.6	82.1	192.9
Fitting to Sakiyama's model eqn (3)				
λ/cm^{-1}	−142	−94	−120	−146
κ	0.93	0.83	0.97	0.86
Δ_{axial}/cm^{-1}	911.2	398.2	920.1	−1594.6
ΔE_1/cm^{-1}	102.1	78.4	78.9	187.5
R	4.5×10^{-5}	1.5×10^{-5}	6.1×10^{-6}	1.8×10^{-5}
HFEPR and FIRMS				
D/cm^{-1}		31.9	33.3	
E/cm^{-1}		0	8.7	
$2D^*$/cm^{-1} [b]		63.8	73.0	140–200
E/D		0	0.26	
g_x,g_y		2.4	2.37	
g_z		2.0	2.10	8.4[c]

[a] $\Delta E_1 = E(\text{KD1}) - E(\text{KD2})$. [b] $2D^* = \Delta E_1 = [2(D^2 + 3E^2)^{1/2}]$. [c] g_{zeff}.

As can be observed in Table 1, compounds **1–3** show easy-plane magnetic anisotropy (both D and Δ_{ax} are positive) in line with that expected for pseudo-octahedral Co^{II} high spin mononuclear complexes with nearly octahedral or compressed tetragonal bipyramid geometries (**2** and **3** have D_{str} values of −1.6 and −7.3, so that the latter geometry is moderately compressed).[27] However, compound **4** exhibits a large axial easy-axis magnetic anisotropy, as expected for trigonal prismatic complexes. It should be noted that except for **3**, the rest of the compounds exhibit a small rhombic anisotropy.

Finally, it is worth noting that the values of the energy gap between the ground and first excited state (ΔE_1) extracted by the three Hamiltonians (Table 1) for each compound are very close. Moreover, these values are slightly higher but compare rather well with those directly extracted by FIRMS.

FIRMS and HFEPR spectroscopy

The zero-field energy gap between the two lowest-energy Kramers doublets (KDs) in an S = 3/2 spin system, as well as the sign and magnitude of the ZFS anisotropy parameters D and E can be in principle extracted from a combination of FIRMS (far-infrared magnetic spectroscopy) and HFEPR (high-frequency and high-field electron paramagnetic spectroscopy). The joint FIRMS and HFEPR maps of turning points as a function of frequency in compounds **2** and **3** (no magnetic transitions could be observed in the spectra of **1**) are shown in Fig. 6. The heat maps represent the FIRMS data while the circles are the HFEPR turning points in the same compounds as seen in Fig. S6.†

From the analysis of the peaks in the normalized FIRMS transmission spectra of compounds **2** and **3** we obtained the following $2D^*$ values (energy gap between the ground and first excited KD in an S = 3/2 system): 63.8 cm^{-1} for **2** and 73 cm^{-1} for **3**. These values were then used for analyzing and simulating the HFEPR spectra of these compounds (Fig. S6†), using a powder pattern typical of an S = 3/2 spin state. Compound **2** produced HFEPR spectra that are significantly distorted, partly by dispersion and by a non-ideal powder distribution, but clearly show that its zfs tensor is axial. The g-values obtained by fitting the frequency/field map of the turning points are given in Table 1. Compound **3**, on the other hand, displayed better-quality spectra that showed a pronounced rhombicity. As usual for an S = 3/2 spin system, it is not possible to differentiate the rhombicity of the zfs tensor and the g-tensor as being responsible.[5o] We thus neglected the rhombicity of the latter, assuming it is axial, and were thus able to estimate the E-value on top of the g-values (see Table 1). It is worth mentioning that it was not possible to simulate the EPR spectra using negative D values. The D values extracted by means of

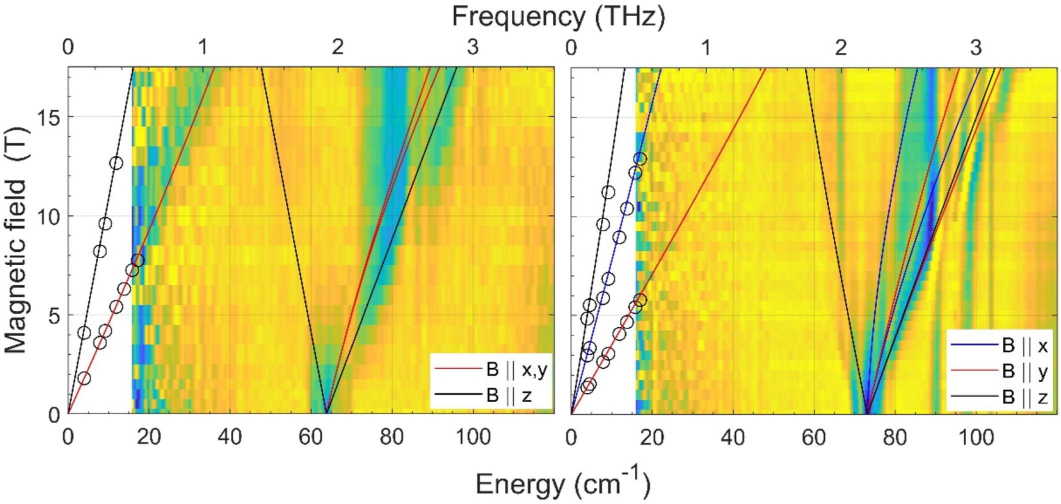

Fig. 6 Experimental (magnetic field *vs.* energy) heat maps of the FIRMS response for complexes **2** (left) and **3** (right). The blue and yellow regions represent resonance absorptions sensitive and insensitive to the field, respectively. The white regions are below the FIRMS sensitivity threshold. The circles represent turning points in the HFEPR spectra. The lines are simulations of those turning points as a function of frequency using the spin Hamiltonian parameters as in Table 1. The meaning of each colour is explained in the labels.

the combined FIRMS/HFEPR methodology for complexes **2** and **3** are very close to those extracted from magnetic data.

For compound **4**, the situation is qualitatively different than for **3** and **4** in terms of magneto-spectroscopic results. The FIRMS heat map of **4** is presented in Fig. S7.† Although there are several zero-field absorption peaks in the frequency range of 130–230 cm^{-1}, none of them can be positively identified as corresponding to the energy gap between the two lowest KDs. The most likely zf magnetic resonance is the strongest one at 210 cm^{-1} but we prefer to estimate the 2D^* value as lying between 130 and 230 cm^{-1}.

The HFEPR spectra of **4** (Fig. S8†) are also very different to those of **2** and **3** and show a single, extremely weak resonance at any frequency positioned at g_{eff} ~8.4. Such a resonance can only be attributed to the parallel turning point $(B||z)$ of the intra-Kramers transition from M_S $|-3/2\rangle$ to $|+3/2\rangle$ within the ±3/2 manifold. It appears in $S = 3/2$ complexes with large negative D values (easy-axis anisotropy) and very small but non-negligible E/D values as has been previously observed in Co$^{\text{II}}$ complexes with a trigonal prismatic coordination sphere, like **4**, and large easy-axis anisotropy, and shows similar HFEPR spectra with g_{zeff} values in the 7–9 range.[31] The perpendicular turning points of the same transition $(B||x, y)$ would occur well outside the field range and therefore were not observed. The transition from $M_s = |-3/2\rangle$ to $|+3/2\rangle$ is forbidden, because it corresponds to $\Delta M_s = \pm 3$ (only transitions with $\Delta M_s = \pm 1$ are allowed), but can be observed because the selection rule is relaxed in the presence of the E-term in the spin Hamiltonian, which mixes the $|\pm 3/2\rangle$ and $|\pm 1/2\rangle$ Kramers doublets. The larger the E, the more allowed the $|-3/2\rangle$ to $|+3/2\rangle$ transition becomes. In the case of **4**, the exceeding weakness of the observed resonance indicates that E is very small with an estimated E/D ratio of less than 0.03. Therefore, in view of the above considerations it is reasonable to assume that **4** must exhibit very large easy-axis anisotropy with a very small E/D value. This assumption is in good agreement with the spin Hamiltonian parameters (D and E) obtained from the fitting of the magnetic data using the ZFS model (Table 1), the FIRMS results (the estimated 2D^* value is very large, between 130 and 230 cm^{-1}), the theoretical calculations (see below) and the spin Hamiltonian parameters found for other Co$^{\text{II}}$ complexes with very large easy-axis anisotropy.[32,50o,p] The fact that the 2D^* value extracted from theoretical calculations is somewhat larger than the higher end of the values determined from FIRMS supports this latter value for D^*.

Theoretical calculations

We have carried out *ab initio* multiconfigurational calculations on the experimental X-ray crystal geometries of complexes **1–4** (*xyz* coordinates for all computed structures are given in Table S6†), using the ORCA 5.0.2 program package,[20] thus obtaining the energy of the spin-free states (Table S7†) and the energy of the KDs generated by the spin–orbit (SO) coupling (Table S8†). This latter interaction was computed by using the quasi-degenerate perturbation theory (QDPT). The calculated D and E values using the ZFS model and first excitation energies before and after including spin–orbit effects for CASSCF and CASSCF + NEVPT2 are given in Table 2. The orientation of the of the D-tensor components are given in Fig. S9.† It can be observed in this table that the computed D and E values for **1**, **2** and **4** are close to those extracted from magnetic data and FIRMS/HFEPR analysis. Nevertheless, the theoretical values are, as usual, larger than those extracted using experimental techniques, which is due to limitations inherent in the calculation methods and the approach based on the ZFS Hamiltonian.

In the case of **3**, CASSCF and CASSCF/NEVPT2 afford D values of the same order of magnitude but of opposite sign.

Table 2 Computed ZFS parameters D, E, $|E/D|$ and g values for the ground state. δE_1 and ΔE_1 are the calculated first excitation energies before and after considering spin–orbit effects, respectively

Compound	Method	D (cm^{-1})	E/D	E (cm^{-1})	δE_1 (cm^{-1})	ΔE_1 (cm^{-1})	g_1, g_2, g_3
1	CASSCF	+98.262	0.119672	11.759	446.0	200.70	1.89, 2.61, 2.87
	CASSCF/NEVPT2	+87.094	0.094115	8.197	615.3	176.49	1.93, 2.60, 2.79
2	CASSCF	+42.738	0.095614	4.086	1263.0	86.64	2.12, 2.48, 2.56
	CASSCF/NEVPT2	+31.796	0.179360	5.703	1658.0	66.59	2.10, 2.37, 2.46
3	CASSCF	+50.136	0.289202	+14.499	1104.3	112.15	2.06, 2.39, 2.69
	CASSCF/NEVPT2	−39.776	0.273560	−10.881	1471.9	88.03	2.06, 2.30, 2.56
4	CASSCF	−123.640	0.066395	−8.209	158.6	248.91	1.68, 1.76, 3.30
	CASSCF/NEVPT2	−121.420	0.052864	−6.419	217.2	243.86	1.74, 1.82, 3.26

These contradictory results are usually observed for mononuclear Co(II) compounds with E/D parameters that are close to 1/3, so that they do not show easy-axis or easy-plane but triaxial anisotropy and the sign of D cannot be unequivocally determined from theoretical calculations based on the ZFS Hamiltonian.[5o] Therefore, in compounds where the sign of D cannot conclusively be obtained from theoretical and magnetic studies, like in **3**, the use of other experimental techniques is mandatory. In this regard, as indicated elsewhere, the HFEPR spectra of **3** (see Fig. S6†) unquestionably demonstrate that $D > 0$ and so the easy-plane anisotropy of the ground state. It is worth noting at this point that, as far as we know, with only one exception, all the Co^{II} complexes with a compressed octahedral CoN$_6$ coordination sphere bearing two thiocyanate anions coordinated in *trans* positions show, like **3**, $D > 0$.[5o,33]

The splitting of the d-orbitals for complexes **1–4** was calculated using the *ab initio* ligand field theory (AILFT) method implemented in ORCA.[34] The computed energy diagrams for these compounds are given in Fig. S10–S13,† whereas the composition of the one-electron states appears in Table S9.† Calculations results indicate that complexes **1–3** and complex **4** show the splitting of the d orbitals expected for pseudooctahedral and distorted trigonal prismatic complexes, respectively. The splitting for compounds **1** and **2** is close to 8800 cm^{-1}, whereas those for compounds **3** and **4** are 11 405 and 9590 cm^{-1}, respectively. The former complexes, which are distorted octahedral, apart from the N-acceptor groups belonging to the ligand, possess π-donor ligands (Cl$^-$ and S) that reduce the magnitude of the ligand-field splitting. However, compounds **3** and **4** possess either π-N-acceptor groups pertaining to the tripodal ligand (aromatic and imine nitrogen atoms) and weak acceptor NCS$^-$ anions for the former or only π-N-acceptor groups belonging to the tripodal ligand for the latter, which favour an increase of the splitting of the d orbitals with regard to **1** and **2**. The fact that the splitting of **3** is larger than that of **4** can be justified because the energy span of the d orbitals in OC-6 complexes is larger than that in the TPR-6 counterparts (10 Dq *vs.* 20/3 Dq).[35]

The splitting of compounds **1–3**, which is typical of distorted octahedral complexes, shows two highly destabilized singly occupied d orbitals ($d_{x^2-y^2}$ and d_{z^2} arising from the e_g system in ideal OC-6 complexes) and three closer energy low-lying d orbitals (d_{xz}, d_{yz}, d_{xy} arising from the t_{2g} systems in OC-6 symmetry). It is worth noting that the highly destabilized orbitals are linear combinations of $d_{x^2-y^2}$ and d_{z^2} (except for **3**, where they can be considered as pure orbitals), whereas the low-lying orbitals are linear combinations of two orbitals of the d_{xz}, d_{yz}, d_{xy} set. In the case of **4**, as expected for a distorted trigonal prismatic geometry, the lowest-lying d orbital is doubly occupied and practically pure d_{z^2}. At higher energy, but relatively close to the lowest-lying d_{z^2} (at 1278 and 1529 cm^{-1}), are found one doubly and one singly occupied orbital, which are essentially a linear combination of both d_{xy} and $d_{x^2-y^2}$ orbitals with either d_{xz} or d_{yz} orbitals, respectively. Finally, at much higher energy (8926 and 9590 cm^{-1}) are located two singly occupied orbitals, which are largely a linear combination of the d_{xz} and d_{yz} orbitals with either d_{xy} or $d_{x^2-y^2}$ orbitals, respectively.

For complexes **1–3**, the two first excited quartet states (see Table S7†) are much lower in energy than the other excited ones. In this regard, the second excited states show energies up to approximately 2300 cm^{-1}, whereas the other excited states are located at energies higher than 5500 cm^{-1}. Therefore, the two low-lying quartet excited states must possess the major contribution to D, because their contributions to this parameter are inversely proportional to their relative energy regarding the ground quartet state. The results of the CASSF/NEVPT2 calculations agree with this hypothesis. In the case of **3**, the CASSF/NEVPT2 calculations led to a wrong sign of D due to the triaxial anisotropy of the ground state (see above). Therefore, the contributions of the excited quartet states to D for **3** have not been included in Table S10.† In the case of **4**, only the first excited state is close to the ground one, as the second excited state is above 4000 cm^{-1}. Therefore, the contribution to D essentially arises from the first excited state (see Table S10†).

Let us at this point undertake a comparative analysis of the D parameters experimentally and theoretically obtained for complexes **1–4** and those published for similar complexes. First, it is important to remark that, when tripodal ligands coordinate in N,N,S-tridentate or bis (N,N-bidentate) forms to the Co^{II} ion, pseudooctahedral Co(II) complexes were obtained, all of them exhibiting positive D values and easy-plane magnetic anisotropy. Specifically, complex **2** and other similar Co^{II}N$_4$Cl$_2$ pseudo-octahedral complexes have been shown to possess easy-plane magnetic anisotropy with D values in the

27–68 cm^{-1} range (except for **2**, in all cases D was extracted from magnetic data and theoretical calculations).[33,36] Moreover, theoretical calculations carried out on the complex $[Co(py)_4Cl_2]$,[33a] by changing the axial and transverse ligand fields and keeping the other structural parameters constant, allowed the establishment of the following magneto-structural correlation: for d_{ax}/d_{eq} ratios <1.02, negative D values are expected, whereas d_{ax}/d_{eq} ratios >1.06 should lead to positive D values. In fact, the $Co^{II}N_4Cl_2$ complexes for which the D parameter has been experimentally determined from the magnetic data exhibit d_{ax}/d_{eq} ratios in the 1.07–1.13 range and all of them, as indicated above, show easy-plane magnetic anisotropy. It is worth mentioning that complex **2** and $[Co(py)_4Cl_2]$ have very close d_{ax}/d_{eq} ratios (1.13 and 1.12, respectively); however, their respective D values extracted from magnetic data are rather separated (34.9 *vs.* 68.2 cm^{-1}, respectively). This fact points out that, besides the axial to equatorial bond length ratio, other structural and electronic factors could also affect the magnitude of the D value. Among the former, one could consider the larger deviations in the coordination sphere of **2** of the *cis* bond angles from 90° (they are found in the 76–114° and 87–93° ranges for **2** and $[Co(py)_4Cl_2]$, respectively), as well as the smaller *trans* Cl–Co–Cl bond angle (168.6 *vs.* 177.4°, respectively).

Regarding complex **3** and its structurally similar $Co^{II}N_6$ pseudo-octahedral complexes bearing two thiocyanate ligands in *trans* positions, all of them exhibit d_{ax}/d_{eq} ratios (d_{ax} and d_{eq} are the average axial and equatorial bond distances, respectively) within the 0.94–0.97 range and D values in the 30–70 cm^{-1} range (most part of them extracted from magnetic data).[32] Theoretical calculations on this type of compressed bipyramidal complex suggest that to achieve negative D values significantly smaller d_{ax}/d_{eq} ratios are required.[37] It should be mentioned that complex **3** and its analogs having pyridyl instead of isoquinolyl moieties in the three arms of the ligand present very close D values (33.3 *vs.* 36.33 cm^{-1}) as expected for their very similar structural parameters in the coordination sphere. Finally, it is worth noting that despite the different d_{ax}/d_{eq} ratios for **2** and **3** (1.13 and 0.97, respectively), they show similar D values, thus indicating that the electronic effects must also play an important role in determining D.

Concerning compound **4**, some of us have shown that there exists a magneto-structural correlation between the continuous shape measures and the experimentally extracted D values for trigonal prismatic Co^{II} complexes with a tripodal ligand analogous to **L** but having a pyridyl moiety instead of an isoquinolyl moiety in each of its arms.[5o] This correlation indicates that the negative D values linearly decrease in absolute value with the increase of the distortion from TPR-6 to OC-6 along the TPR-6 ↔ OC6 deformation pathway. Using this linear correlation and the S(TPR-6) value for **4** of 4.322, the calculated D value would be much smaller than that found from magnetic data, FIRMS/HFEPR and theoretical calculations. This result suggests that, even though the S(TPR-6) is an essential factor in determining the sign and magnitude of D, other structural factors (compression and truncation of the trigonal prismatic geometry) and the electronic effects of the donor atoms of the ligand should also influence the final value of D.

Dynamic magnetic properties

The dynamics of the magnetization for complexes **1–4** was analysed by carrying out temperature and frequency dependence studies of the ac magnetic susceptibility under an alternating field of either 5 Oe or 10 Oe on polycrystalline samples of the compounds. The aim of this analysis is to disclose if these compounds show slow magnetization relaxation and, if so, to perform a comparative study of their dynamic magnetic properties with those previously reported for closely structurally related Co^{II} complexes. Unfortunately, complexes **1–3** do not show out-of-phase signals (χ''_M) above 2 K at zero applied dc field. This result is not surprising because for Co^{II} Kramers ions with easy-plane anisotropy, the electronuclear spin states arising from the hyperfine interactions between the electronic and nuclear spins have negligible magnetic moments under zero magnetic field and, consequently, they do not show slow magnetic relaxation. Therefore, to observe the potentially slow relaxation of the magnetization in this type of complexes it would be mandatory to apply a magnetic field.[38] In addition, calculations with the SINGLE-ANISO code implemented in the ORCA 5.0.2 program package (ESI†) show that QTM in the ground state cannot be ruled out for **1–3**, because the matrix element for the QTM transition is significantly larger than 0.1, which is assumed as the minimum value needed for an efficient relaxation mechanism (Fig. S14–S17†).[39]

Compound **4**, under a zero applied magnetic field, shows χ''_M signals below 10 K, but without reaching maxima even at the highest used frequency of 10 000 Hz (Fig. S18†). This behaviour could be due to QTM promoted by the existence of transverse anisotropy (theoretical calculations show that compound **4** has a slight but non-negligible transverse magnetic anisotropy, see Table 2), weak dipolar interactions and hyperfine interactions with the Co^{II} nuclear spin (I = 7/2). In fact, SINGLE-ANISO calculations support the existence of QTM, because the matrix element for the QTM transition is 0.12 (Fig. S17†). Moreover, the relatively significant distortion of the molecules of **4** from TPR-6 to OC-6 geometry favours the appearance of significant QTM. In view of the above considerations, one realizes why QTM is generally hard to quench enough so as to detect slow relaxation under zero-field.

To eliminate fully or partly the QTM in complexes **1–4**, ac measurements in the presence of small dc fields were performed. For complex **1** no χ''_M signals were observed at the tested magnetic fields in the 0–3000 Oe range, whereas **2–4** show frequency and temperature dependence of the out-of-phase signals under an applied magnetic field and, therefore, slow relaxation of the magnetization (Fig. S19–S21†). Using the data corresponding to the field and frequency dependence of χ''_M at 2 K for **2** and **3** and 6 K for **4**, the optimal field for the ac measurements were determined for each of the compounds. In the case of **2** and **3**, the relaxation times could not be accurately extracted from the fitting of the frequency dependence of the χ''_M signals to the generalized Debye model, because the maxima appear beyond the frequency limit of our apparatus. Therefore, the field giving rise to the maximum intensity of the χ''_M signals was the choice. For **4**, the field dependence of the relaxation time in form of τ^{-1} *vs.* H (in tesla units) is given in Fig. S21† (right panel). As expected, the magnetic relaxation slows down up to 0.15 T (this optimal field agrees well with that at which the intensity of the χ''_M signals is maximal) due to the progressive quenching of the QTM. For $H_{dc} > 0.15$ T, τ^{-1} slightly increases as the field increases, due to a small contribution, if one exists, of a direct relaxation process, which would be strongly field dependent. A full set of temperature- and frequency-dependent ac susceptibility measurements were then carried out at the corresponding optimal fields for **2–4** below 15 K (Fig. 7, respectively).

As can be seen in these figures, the three compounds show a clear frequency dependence of the χ''_M signals at different temperatures, thus pointing out the existence of slow magnetic relaxation. From these data and using the generalized Debye model, the temperature dependence of the relaxation time was extracted for **2–4**, which is given in Fig. 8.

The τ^{-1} *vs.* T is generally described by the following equation:

$$\tau^{-1} = AH^4T + \frac{B_1}{1+B_2H^2} + CT^n + \tau_0 \exp\left(-\frac{U_{\mathrm{eff}}}{k_BT}\right) \qquad (4)$$

where the two first terms represent the field dependent direct and QTM relaxation processes, respectively, whereas the third and fourth terms describe the field-independent Raman and Orbach relaxation processes. The high-temperature region of the τ^{-1} *vs.* T data for **2–4** seems to obey the Arrhenius law (Fig. S22†) with U_{eff} and τ_0 values of 6.88(9) K and 3.95(8) × 10^{-6} s, respectively, for **2**, 24(3) K and 3(3) × 10^{-7} s, respectively, for **3** and 30(2) K and 4(1) × 10^{-6} s, respectively, for **4**. These U_{eff} values are much lower than the $|2D^*|$ (energy gap between the ground and first excited states) values extracted from *ab initio* theoretical calculations, experimental susceptibility and magnetization dc data and FIRMS results for **2–4** ($|2D^*| \sim 70$–80 cm^{-1} for **2** and **3** and ~200 cm^{-1} for **4**). Therefore, the Orbach process, which takes place through real states, could be discarded for **2–4**. The α values extracted from the Cole–Cole plot for compounds **2–4** (Fig. S23–S25†) in the 4–8 K region are very small (~0.10 for **2** and **3** and 0.05 for **4**) and the curves have a semicircular shape, thus pointing out the operation of a unique relaxation process (Raman process).

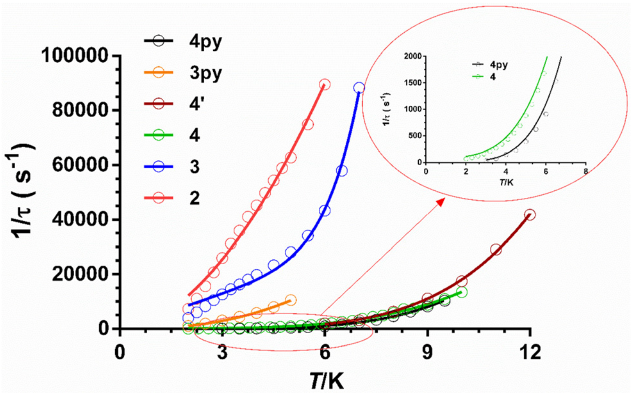

Fig. 8 Temperature dependence of the inverse of the relaxation times for the indicated compounds at the corresponding optimal fields. Solid lines represent the best fits to the relaxation processes specified in the text.

Nevertheless, below 4 K, the α values increase until they reach values of 0.2, 0.4 and 0.2 at 2 K for **2–4**, respectively, which indicates the existence of a wide distribution of relaxation times, particularly in the case of compounds **3** and **4**. This dynamic behavior is in agreement with the existence of various overlapping relaxation processes at a very low temperature (Raman, field-induced direct, and eventually QTM if the applied field does not fully quench it). In view of this, the $1/\tau$ *vs.* T data were fitted to: (i) a Raman process for **2** (the fit worsens when the direct process is also taken into consideration), (ii) a combination of Raman and direct processes for **3** and (iii) a combination of Raman, direct and QTM for **4**. The QTM contribution has been considered for **4**, because the temperature dependence of the χ''_M signals at different frequencies shows that the curves do not tend to zero after the maxima at a very low temperature (see Fig. S26†). This contribution is likely to be due to hyperfine interactions, opening channels for fast relaxation. In the case of **4** the A, B_1 and B_2 parameters in eqn (4) were fixed to the values extracted from the field dependence of the relaxation time (Fig. S21† right). The best-fit parameters extracted for compounds **2–4** are gathered in Table 3. It is worth mentioning that even though for Kramers ions a n value of 9 would be expected,[40] lower n values can be taken as acceptable depending on the structure of the levels, and if both acoustic and optical phonons are considered.[41]

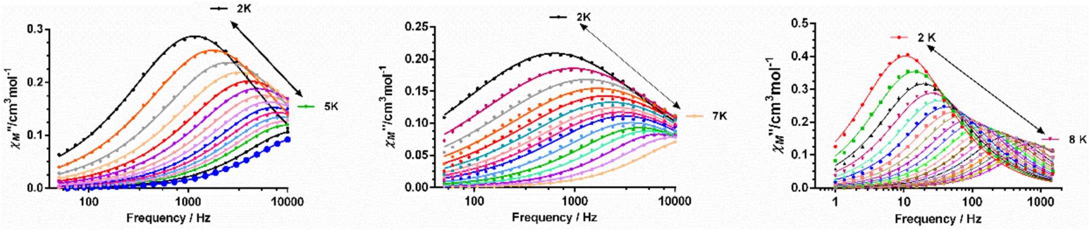

Fig. 7 Frequency dependence of the out-of-phase signals (χ''_M) at the indicated temperature ranges and under the optimal fields of 0.12 T for **2** (left) and **3** (centre) and 0.15 T (right) for **4**. Solid lines represent the best-fit curves to the generalized Debye model.

Table 3 Magnetic relaxation parameters for complexes **1–4**

Compound	U_{eff} (K)	τ_0 (s)	C (s^{-1} K^{-n})	n	QTM/s	A (s^{-1} T^{-4} K^{-1})
2	6.88(9)	$3.95(8) \times 10^{-6}$	2866 (330), H = 0.12 T	1.94(8)	—	—
3	24(3) K	$3.(3) \times 10^{-7}$	0.03 (4), H = 0.12 T	7.4(7)	—	4290(260)
4	30.2(4)	$4(1) \times 10^{-6}$	1.6 (2), H = 0.15 T	3.93(5)	0.013	—
4′	43(1)	$6.7(3) \times 10^{-7}$	0.4 (1), H = 0 T	4.6(1)	—	—

It is worth mentioning that some mononuclear Co$^{\text{II}}$ complexes, even though they have large easy-axis magnetic anisotropy in the ground state, do not present slow magnetic relaxation and SIM behaviour at zero field. This behaviour is likely due to intermolecular interactions that promote fast QTM. Nevertheless, in these systems, the slow magnetic relaxation could be activated by magnetic dilution of the pristine compound, because this process could quench the intermolecular magnetic interactions.[42,5o] In light of this, we decided to explore if **4′** (the diluted version of **4**) would present dilution-triggered slow magnetic relaxation. Compound **4′** presents a Co/Zn = 1/10 ratio, which was supported by dc magnetic measurements. Although the powder X-ray diffractogram is silent, the IR and mass spectra (ESI-MS) point out that **4′** is pure and potentially amorphous, yet equivalent to **4**. Temperature- and frequency-dependence ac magnetic measurements under zero field of **4′** (Fig. S27†) display χ''_{M} signals with maxima in the 6 K (330 Hz)–12 K (6800 Hz) range, typical of slow magnetization relaxation. Therefore, compound **4′** exhibits dilution-induced slow-magnetic relaxation at zero applied field ("hidden SIM" behaviour). The temperature dependence of relaxation times for **4′** (Fig. 8) was analysed with an equation that only considers the existence of the Raman process (under zero magnetic field the direct product should be negligible and the typical tail due to QTM does not appear in the low-temperature region). Moreover, for comparative purposes, the phenomenological U_{eff} values were extracted from the fitting of the linear high-temperature region of the Arrhenius plots. As expected, the U_{eff} value is quite lower than the $2D^*$ value determined from magnetic, theoretical calculations and FIRMS. The parameters extracted from these two fittings are given in Table 3.

From the magnetic relaxation parameters gathered in Table 3 and Fig. 8, we can highlight the following facts: (i) in spite of the fact that compound **3** and its analogue containing pyridine instead of isoquinoline moieties, **3Py** (compound **11** in Fig. 4), present very similar SHAPE parameters and D values; however, the former relaxes considerably faster than the latter. (ii) Although the D values for **4** and **4py** (compound **7** in Fig. 4) extracted from FIRMS are very similar, the former relaxes faster than **4py**. In this case, the slightly larger distortion from the ideal TPR-6 geometry for **4** compared with **4py** might lead to a lower axiality of the ground and, therefore, to contributing in some extent to the decrease of the relaxation time for the former. (iii) Compound **4** at the optimal field relaxes more slowly than **4′** at the zero field, pointing out once again that the effect of the applied dc field for quenching QTM is larger than that coming from the magnetic dilution. Points (i) and (ii) suggest that the change of the pyridine moiety by the isoquinoline one in the tripodal ligand is essentially responsible for the faster magnetization relaxation observed for **3** and **4** with respect to their closely related **3y** and **4py** counterparts, respectively. Several recent exciting papers have theoretically clarified the crucial role played by the molecular and lattice vibrations coupled with the electronic spins in the magnetic relaxation of SMMs.[43] Some of them specifically dealing with Co$^{\text{II}}$ SIMs have revealed that low-energy phonons (the most populated at the low experimental temperatures) can couple with the spin inducing spin-relaxation at low temperatures through anharmonic Orbach and/or Raman mechanisms, which restricts the spin lifetime.[43a,h,j] Therefore, to build efficient SMMs, static magnetism (controlling the crystal field to increase the single-ion anisotropy and quenching of QTM by strong magnetic coupling between magnetic centres or magnetic dilution) and spin-phonon dynamics (engineering of molecular vibrations) have to be parallel tuned. In connection with this, it was found that the spin dynamics of some linear Fe$^{\text{II}}$ SIMs was accelerated upon increasing their molecular size, even though they possessed a similar computed energy gap between the ground and first excited states.[44] This result highlights the impact of the molecular dimensions on the magnetic relaxation dynamics, which can be explained by the increase of the delocalization of the vibrational modes in the low-energy vibrational spectra when the molecular dimensions increase, thus ultimately favouring the coupling of the spin and the low-energy phonons. The above considerations support that the acceleration of the magnetic relaxation in compounds **3** and **4** regarding **3py** and **4y** is most likely due to the increase of the molecular size due to the replacement of the pyridine moiety by the bulkier isoquinoline one.

Conclusions

The ongoing results demonstrate that using the tripodal ligand prepared by the condensation of $S{=}P(NHCH_3\text{-}NH_2)_3$ and 2-quinolinecarboxaldehyde, a mononuclear distorted octahedral Co$^{\text{II}}$ complex with a CoN$_4$SO coordination sphere is obtained, where the ligand is forced, due to the steric hindrance between the quinoline moieties belonging to the three arms, to adopt a N,N,S-tridentate coordination mode instead of the expected N$_6$-trisbidentate tripodal one. However, when a non-sterically hindered tripodal ligand bearing isoquinolyl substituents is used, depending on the coordination ability of the anion, mononuclear complexes are obtained where the ligand acts with either bisbidentate or trisbidentate coordination modes. Thus, utilizing good coordinating anions, such as SCN^- or Cl^-, tetragonally distorted $Co^{II}N_4X_2$ complexes (X = Cl^- or NCS^-) are obtained where the anions are in *trans* positions in the Co^{II} coordination sphere, whereas the four nitrogen atoms of the bisbidentate ligand occupy the equatorial positions. However, using poor coordinating perchlorate anions, the ligand can coordinate to the Co^{II} ion in a N_6-trisbidentate tripodal coordination mode, giving rise to a distorted trigonal prismatic CoN_6 coordination sphere.

Magnetic measurements, theoretical calculations, FIRMS and EPR show that the distorted octahedral complexes exhibit positive axial anisotropy parameters ($D > 0$), which are larger for **1** (from magnetic measurements and theoretical calculations) than for **2** and **3**. This behaviour is not unexpected as most of this type of complex exhibit $D > 0$ values. For complexes **2** and **3** the comparative analysis of their magneto-structural data with those found for other similar complexes allows the conclusion that besides the axial to equatorial bond length ratio, other structural and electronic factors must also affect the magnitude of the D value. In contrast to the distorted octahedral complexes, the distorted trigonal prismatic complex **4** shows, as expected, a large easy-axis magnetic anisotropy ($D < 0$). When the D value for **4** is compared with those of closely related trigonal prismatic Co^{II} complexes, one realizes that even though the distortion from the ideal TPR-6 geometry is an essential factor in determining the sign and magnitude of D, other structural factors (compression and truncation of the trigonal prismatic geometry) and the electronic effects of the donor atoms of the ligand should also influence the final value of D.

Theoretical calculations carried out on compounds **1–4** support that QTM precludes the observation of slow relaxation at zero-field in these compounds. However, compounds **2–4** exhibit field-induced slow relaxation and the temperature dependence of the relaxation time for these compounds can be fitted to a Raman mechanism for the former, Raman and direct ones for the second and Raman, direct and QTM mechanisms for the latter. In all cases, above 3–4 K the Raman is the dominant process. It is of interest that slow relaxation can be observed at zero field for compound **4** after magnetic dilution with Zn^{II}, which quenches the QTM promoted by the intermolecular dipolar interactions. This behaviour is not unexpected in view of its large easy-axis magnetic anisotropy.

Finally, interestingly enough, the magnetic relaxations of **3** and **4** are comparatively faster than those of the analogous compounds bearing pyridine as a substituent in their arms, which appears to be most likely due to the increase of the molecular size due to the replacement of the pyridine moiety by the bulkier isoquinoline one.

Conflicts of interest

There are no conflicts of interest to declare.

Acknowledgements

Financial support from the Ministerio de Ciencia e Innovación (project PID2022-138090NB-C21 funded by MCIN/AEI/10.13039/501100011033/FEDER,UE), Junta de Andalucía (FQM-195 and project I+D+i P20_00692), and the University of Granada are grateful acknowledged. The authors acknowledge the Centro de Servicios de Informática y Redes de Comunicaciones (CSIRC) for computational time and facilities. M. M. Q. M. thanks Junta de Andalucía for a postdoctoral fellowship (DOC_01282) and Ministerio de Ciencia e Innovación for a Ramón y Cajal contract (the publication is part of the grant RYC2021-034288-I, funded by MCIN/AEI/10.13039/501100011033 and by the European Union "NextGenerationEU"/PRTR"). Part of this work was performed at the NHMFL, which is funded by the National Science Foundation (cooperative agreement DMR 2128556) and the State of Florida. The authors are grateful to Dr M. Quirós from University of Granada for his help in the crystal structures resolution.

References

1 (*a*) D. Gatteschi and R. Sessoli, *Angew. Chem., Int. Ed.*, 2003, **42**, 268; (*b*) D. Gatteschi, R. Sessoli and J. Villain, *Molecular nanomagnets*, Oxford University Press, Oxford, 2006; (*c*) J. Bartolomé, F. Luis and J. F. Fernández, *Molecular magnets: physics and applications*, Springer-Verlag, Berlin-Heidelberg, 2014; (*d*) G. A. Craig and M. Murrie, *Chem. Soc. Rev.*, 2015, **44**, 2135; (*e*) Y.-S. Ming, S. D. Jiang, B.-W. Wang and S. Gao, *Acc. Chem. Res.*, 2016, **49**, 2381; (*f*) A. Day, P. Kalita and V. V. Chandrasekhar, *ACS Omega*, 2018, **2108**(20), 942; (*g*) M. Fen and M.-L. Tong, *Chem. – Eur. J.*, 2018, **24**, 7574; (*h*) A. Sarkar, S. Dey and G. Rajaraman, *Chem. – Eur. J.*, 2020, **26**, 14036; (*i*) A. Zabala-Lekuona, M. Seco and E. Colacio, *Coord. Chem. Rev.*, 2021, **441**, 213984; (*j*) J. Juráková and I. Šalitroš, *Monatsh. Chem.*, 2022, **153**, 1001; (*k*) N. F. Chilton, *Annu. Rev. Mater. Res.*, 2022, **52**, 79; (*l*) P. K. Sahu, R. Kharel, S. Shome, S. Goswami and S. Konar, *Coord. Chem. Rev.*, 2023, **475**, 2148714.

2 E. Moreno-Pineda and W. Wernsdorfer, *Nat. Rev. Phys.*, 2021, **3**, 645.

3 (*a*) C. A. P. Goodwin, F. Ortu, D. Reta, N. F. Chilton and D. P. Mills, *Nature*, 2017, **548**, 439; (*b*) F. S. Guo, B. M. Day, Y. C. Chen, M. L. Tong, A. Mansikkamäki and R. A. Layfield, *Angew. Chem., Int. Ed.*, 2017, **56**, 11445; (*c*) F. S. Guo, B. M. Day, Y. C. Chen, M. L. Tong, A. Mansikkamäki and R. A. Layfield, *Science*, 2018, **362**, 1400.

4 (*a*) X. N. Yao, J. Z. Du, Y. Q. Zhang, X. B. Leng, M. W. Yang, S. D. Jiang, Z. X. Wang, Z. W. Ouyang, L. Deng, B. W. Wang and S. Gao, *J. Am. Chem. Soc.*, 2017, **139**, 373; (*b*) P. C. Bunting, M. Atanasov, E. Damgaard-Møller,

M. Perfetti, I. Crassee, M. Orlita, J. Overgaard, J. van Slageren, F. Neese and J. R. Long, *Science*, 2018, **362**, 7319.

5 (*a*) S. Gómez-Coca, E. Cremades, N. Aliaga-Alcalde and E. Ruiz, *J. Am. Chem. Soc.*, 2013, **135**, 7010; (*b*) A. A. Pavlov, Y. V. Nelyubina, S. V. Kats, L. V. Penkova, N. N. Efimov, A. O. Dmitrienko, A. V. Vologzhanina, A. S. Belov, Y. Z. Voloshin and V. V. J. Novikov, *Phys. Chem. Lett.*, 2016, **7**, 4111; (*c*) Y. Y. Zhu, Y. Q. Zhang, T. T. Yin, C. Gao, B. W. Wang and S. Gao, *Inorg. Chem.*, 2015, **54**, 5475; (*d*) Y. Y. Zhu, C. Cui, Y. Q. Zhang, J. H. Jia, X. Guo, C. Gao, K. Qian, S. D. Jiang, B. W. Wang, Z. M. Wang and S. Gao, *Chem. Sci.*, 2013, **4**, 1802; (*e*) T. J. Ozumerzifon, I. Bhowmick, W. C. Spaller, A. K. Rappé and M. P. Shores, *Chem. Commun.*, 2017, **53**, 4211; (*f*) Y. Peng, T. Bodenstein, K. Fink, V. Mereacre, C. E. Anson and A. K. Powell, *Phys. Chem. Chem. Phys.*, 2016, **18**, 30135; (*g*) B. Yao, Y. F. Deng, T. Li, J. Xiong, B. W. Wang, Z. Zheng and Y. Y. Zhang, *Inorg. Chem.*, 2018, **57**, 14047; (*h*) V. V. Novikov, A. A. Pavlov, Y. V. Nelyubina, M. E. Boulon, O. A. Varzatskii, Y. Z. Voloshin and R. E. P. Winpenny, *J. Am. Chem. Soc.*, 2015, **137**, 9792; (*i*) A. A. Pavlov, D. Y. Aleshin, S. A. Savkina, A. S. Belov, N. N. Efimov, J. Nehrkorn, M. Ozerov, Y. Z. Voloshin, Y. V. Nelyubina and V. V. Novikov, *ChemPhysChem*, 2019, **20**, 1001; (*j*) C. Villa-Pérez, I. Oyarzabal, G. A. Echeverría, G. C. Valencia-Uribe, J. M. Seco and D. B. Soria, *Eur. J. Inorg. Chem.*, 2016, 4835; (*k*) C. M. Klug, T. J. Ozumerzifon, I. Bhowmick, B. N. Livesay, A. K. Rappé and M. P. Shores, *Dalton Trans.*, 2019, **48**, 9117; (*l*) A. A. Pavlov, S. A. Savkina, A. S. Belov, Y. V. Nelyubina, N. N. Efimov, Y. Z. Voloshin and V. V. Novikov, *Inorg. Chem.*, 2017, **56**, 6943; (*m*) A. S. Belov, Y. Z. Voloshin, A. A. Pavlov, Y. V. Nelyubina, S. A. Belova, Y. V. Zubavichus, V. V. Avdeeva, N. N. Efimov, E. A. Malinina, K. Y. Zhizhin and N. T. Kuznetsov, *Inorg. Chem.*, 2020, **59**, 5845; (*n*) M. R. Saber, M. K. Singh and K. R. Dunbar, *Chem. Commun.*, 2020, **56**, 8492; (*o*) A. Landart-Gereka, M. M. Quesada-Moreno, I. F. Díaz-Ortega, H. Nojiri, M. Ozerov, J. Krzystek, M. A. Palacios and E. Colacio, *Inorg. Chem. Front.*, 2022, **9**, 2810; (*p*) A. Landart-Gereka, M. M. Quesada-Moreno, M. A. Palacios, I. F. Díaz-Ortega, H. Nojiri, M. Ozerov, J. Krzystek and E. Colacio, *Chem. Commun.*, 2023, **59**, 952.

6 A. Zabala-Lekuona, A. Landart-Gereka, M. M. Quesada-Moreno, A. J. Mota, I. F. Díaz-Ortega, H. Nojiri, J. Krzystek, J. M. Seco and E. Colacio, *Inorg. Chem.*, 2023, **62**(49), 20030.

7 M. W. Löble, M. Casimiro, D. T. Thielemann, P. Oña-Burgos, I. Fernandez, P. W. Roesky and F. Breher, *Chem. – Eur. J.*, 2012, **18**, 5325.

8 J. Nehrkorn, J. Telser, K. Holldack, S. Stoll and A. Schnegg, *J. Phys. Chem. B*, 2015, **119**, 13816.

9 S. Stoll and A. Schweiger, *J. Magn. Reson.*, 2006, **178**, 42.

10 A. K. Hassan, L. A. Pardi, J. Krzystek, A. Sienkiewicz, P. Goy, M. Rohrer and L. C. Brunel, *J. Magn. Reson.*, 2000, **142**, 300–312.

11 *APEX2*, Bruker AXS, Madison, WI, 2010.

12 *SAINT, Version 8.30a*, Bruker AXS, Madison, WI, 2013.

13 G. M. Sheldrick, *SADABS, Version 2004/1*, Bruker AXS, Madison, WI, 2008.

14 G. M. Sheldrick, *Acta Crystallogr., Sect. A: Found. Crystallogr.*, 2008, **64**, 112.

15 G. M. Sheldrick, *Acta Crystallogr., Sect. A: Found. Adv.*, 2015, **71**, 3.

16 G. M. Sheldrick, *Acta Crystallogr., Sect. C: Struct. Chem.*, 2015, **71**, 3.

17 O. V. Dolomanov, L. J. Bourhis, R. J. Gildea, A. K. Howard and H. Pushman, *J. Appl. Crystallogr.*, 2009, **42**, 339.

18 P. A. Malmqvist and B. O. Roos, *Chem. Phys. Lett.*, 1989, **155**, 189.

19 (*a*) C. Angeli, R. Cimiraglia and J.-P. Malrieu, *Chem. Phys. Lett.*, 2001, **350**, 297; (*b*) C. Angeli, R. Cimiraglia, S. Evangelisti, T. Leininger and J.-P. Malrieu, *J. Chem. Phys.*, 2001, **114**, 10252; (*c*) C. Angeli, R. Cimiraglia and J.-P. Malrieu, *J. Chem. Phys.*, 2002, **117**, 9138.

20 (*a*) F. Weigend and R. Ahlrichs, *Phys. Chem. Chem. Phys.*, 2005, **7**, 3297; (*b*) A. Schaefer, H. Horn and R. Ahlrichs, *J. Chem. Phys.*, 1992, **97**, 2571; (*c*) A. Schaefer, C. Huber and R. Ahlrichs, *J. Chem. Phys.*, 1994, **100**, 5829.

21 F. Neese, *Wiley Interdiscip. Rev.: Comput. Mol. Sci.*, 2022, **12**, e1606.

22 (*a*) D. Ganyushin and F. Neese, *J. Chem. Phys.*, 2013, **138**, 104113; (*b*) D. Ganyushin and F. Neese, *J. Chem. Phys.*, 2006, **125**, 024103; (*c*) R. Maurice, R. Bastardis, C. D. Graaf, N. Suaud, T. Mallah and N. Guihéry, *J. Chem. Theory Comput.*, 2009, **5**, 2977; (*d*) F. Neese, *J. Chem. Phys.*, 2005, **122**, 034107.

23 T. Nakajima, *Chem. Rev.*, 2012, **112**, 385.

24 J. Jung, M. Atanasov and F. Neese, *Inorg. Chem.*, 2017, **56**, 8802.

25 V. Chandrasekhar, M. D. Pandey, K. Gopal and R. Azhakar, *Dalton Trans.*, 2011, **40**, 7873.

26 (*a*) M. Llunell, D. Casanova, J. Cirera, P. Alemany and S. Alvarez, *SHAPE, v2.1*, Universitat de Barcelona, Barcelona, Spain, 2013; (*b*) J. Moncol, *Czech Chem. Soc. Symp. Ser.*, 2023, **21**, 147.

27 R. Boca, C. Rajnák and J. Titis, *Magnetochemistry*, 2023, **9**, 100.

28 (*a*) B. N. Figgis and M. A. Hitchman, *Ligand Field Theory and its Applications*, Wiley-VCH, New York, USA, 2000; (*b*) F. Lloret, M. Julve, J. Cano, R. Ruiz-García and E. Pardo, *Inorg. Chim. Acta*, 2008, **316**, 3432.

29 (*a*) J. Juráková, J. D. Midlíková, J. Hrubý, A. Kliuikov, V. T. Santana, J. Pavlik, J. Moncol, E. Čižmár, M. Orlita, I. Mohelský, P. Neugebauer, D. Gentili, M. Cavallini and I. Šalitroš, *Inorg. Chem. Front.*, 2022, **9**, 1179; (*b*) N. Malinová, J. Juráková, B. Brachňaková, J. D. Midlíková, E. Čižmár, V. N. Santana, R. Herchel, M. Orlita, I. Mohelský, J. Moncol, P. Neugebauer and I. Šalitroš, *Cryst. Growth Des.*, 2023, **23**(4), 2430.

30 (*a*) N. F. Chilton, R. P. Anderson, L. D. Turner, A. Soncini and K. S. Murray, *J. Comput. Chem.*, 2013, **34**, 1164; (*b*) H. Sakiyama, *J. Chem. Software*, 2001, **7**(4), 171.

31 (*a*) S. Sottini, G. Poneti, S. Ciattini, N. Levesanos, E. Ferentinos, J. Krzystek, L. Sorace and P. Kyritsis, *Inorg. Chem.*, 2016, **55**, 9537–9548; (*b*) J. R. Pilbrow, *J. Magn. Reson.*, 1978, **31**, 479–490.

32 (*a*) H.-H. Cui, Y.-Q. Zhang, X.-T. Chen, Z. Wang and Z.-L. Xue, *Dalton Trans.*, 2019, **48**, 10743–10752; (*b*) P. Cucos, F. Tuna, L. Sorace, I. Matei, C. Maxim, S. Shova, R. Gheorghe, A. Caneschi, M. Hillebrand and M. Andruh, *Inorg. Chem.*, 2014, **53**, 7738–7747.

33 (*a*) Y.-F. Deng, M. K. Singh, D. Gan, T. Xiao, Y. Wang, S. Liu, Z. Wang, Z. Ouyang, Y.-Z. Zhang and K. R. Dunbar, *Inorg. Chem.*, 2020, **59**, 7622; (*b*) P. Zoufalý, A. Kliuikov, E. Čižmár, I. Císařová and R. Herchel, *Eur. J. Inorg. Chem.*, 2021, 1190; (*c*) J. Vallejo, F. R. Fortea-Pérez, E. Pardo, S. Benmansour, I. Castro, J. Krzystek, D. Armentano and J. Cano, *Chem. Sci.*, 2016, **7**, 2286; (*d*) Y. Y. Zhu, M. S. Zhu, T. T. Yin, Y. S. Meng, Z. Q. Wu, Y. Q. Zhang and S. Gao, *Inorg. Chem.*, 2015, **54**, 3716; (*e*) G. Brunet, D. A. Safin, J. Jover, E. Ruiz and M. Murugesu, *J. Mater. Chem. C*, 2017, **5**, 835.

34 E. A. Suturina, J. Nehrkorn, J. M. Zadrozny, J. Liu, M. Atanasov, T. Weyhermüller, D. Maganas, S. Hill, A. Schnegg, E. Bill, J. R. Long and F. Neese, *Inorg. Chem.*, 2017, **56**, 3102.

35 J. C. Knight, S. Alvarez, A. J. Amoroso, P. G. Edwards and N. Singha, *Dalton Trans.*, 2010, **39**, 3870.

36 L. Shi, F.-X. Shen, D. Shao, Y.-Q. Zhang and X.-Y. Wang, *CrystEngComm*, 2019, **21**, 3176.

37 S. Tripathi, S. Vaidya, N. Ahmed, E. A. Klahn, H. Cao, L. Spillecke, C. Koo, S. Spachmann, R. Klingeler, G. Rajaraman, J. Overgaard and M. Shanmugam, *Cell Rep. Phys. Sci.*, 2021, **2**, 100404.

38 S. Gómez-Coca, A. Urtizberea, E. Cremades, P. J. Alonso, A. Camón, E. Ruiz and F. Luis, *Nat. Commun.*, 2014, **5**, 4300.

39 S. Gómez-Coca, D. Aravena, R. Morales and E. Ruiz, *Coord. Chem. Rev.*, 2015, **289–290**(1), 379.

40 A. Abragam and B. Bleaney, *Electron Paramagnetic Resonance of Transition Ions*, Dover, 1970.

41 (*a*) A. Singh and K. N. Shrivastava, *Phys. Status Solidi B*, 1979, **95**, 273; (*b*) K. N. Shirivastava, *Phys. Status Solidi B*, 1983, **117**, 437.

42 (*a*) J. Li, Y. Han, F. Cao, R.-M. Wei, Y.-Q. Zhang and Y. Song, *Dalton Trans.*, 2016, **45**, 9279; (*b*) R. Mitsuhashi, S. Hosoya, T. Suzuki, Y. Sunatsuki, H. Sakiyama and M. Mikuriya, *RSC Adv.*, 2020, **10**, 43472; (*c*) L. Rigamonti, N. Bridonneau, G. Poneti, L. Tesi, L. Sorace, D. Pinkowicz, J. Jover, E. Ruiz, R. Sessoli and A. Cornia, *Chem. – Eur. J.*, 2018, **24**, 8857; (*d*) S. Sottini, G. Poneti, S. Ciattini, N. Levesanos, E. Ferentinos, J. Krzystek, L. Sorace and P. Kyritsis, *Inorg. Chem.*, 2016, **55**, 9537.

43 (*a*) A. Lunghi and S. Sanvito, *J. Chem. Phys.*, 2020, **153**, 174113; (*b*) A. Lunghi and S. Sanvito, *Sci. Adv.*, 2019, **5**, eaax7163; (*c*) A. Albino, S. Benci, M. Atzori, L. Chelazzi, S. Ciattini, A. Taschin, P. Bartolini, A. Lunghi, R. Righini and R. Torre, *J. Phys. Chem. C*, 2021, **125**, 22100; (*d*) Z. Hu, A. Ullah, H. Prima-Garcia, S.-H. Chin, Y. Wang, J. Aragó, Z. Shi, A. Gaita-Ariño and E. Coronado, *Chem. – Eur. J.*, 2021, **27**, 13242; (*e*) M. Briganti, F. Santanni, L. Tesi, F. Totti, R. Sessoli and A. Lunghi, *J. Am. Chem. Soc.*, 2021, **143**, 13633; (*f*) J. M. Zadrozny, M. Atanasov, A. M. Bryan, C.-Y. Lin, B. D. Rekken, P. P. Power, F. Neese and J. R. Long, *Chem. Sci.*, 2013, **4**, 125; (*g*) F. S. Santana, M. Perfetti, M. Briganti, F. Sacco, G. Poneti, E. Ravera, J. F. Soares and R. Sessoli, *Chem. Sci.*, 2022, **13**, 580; (*h*) D. H. Moseley, S. E. Stavretis, K. Thirunavukkuarasu, M. Ozerov, Y. Cheng, L. L. Daemen, J. Ludwig, Z. Lu, D. Smirnov, C. M. Brown, A. Pandey, A. J. Ramirez-Cuesta, A. C. Lamb, M. Atanasov, E. Bill, F. Neese and Z. L. Xue, *Nat. Commun.*, 2018, **9**, 2572; (*i*) F. S. Santana, M. Perfetti, M. Briganti, F. Sacco, G. Poneti, E. Ravera, J. F. Soares and R. Sessoli, *Chem. Sci.*, 2022, **13**, 5860; (*j*) S. Nain, M. Kumara and Md. E. Ali, *Phys. Chem. Chem. Phys.*, 2023, **25**, 14848; (*k*) A. Castro-Alvarez, Y. Gil, L. Llanos and D. Aravena, *Inorg. Chem. Front.*, 2020, **7**, 2478.

44 A. Lunghi, F. Totti, S. Sanvito and R. Sessoli, *Chem. Sci.*, 2017, **8**, 6051.